(Project Number: 945 041)

DELIVERABLE D2.6

Advanced Manufacturing Processes and Materials

Lead Beneficiary: USFD

Due date: 30/06/2024 Released on: 28/06/2024

Authors:	Jana Kalivodova, Udisien Woy, Jarosław Jasiński, Tomasz Stasiak, Łukasz Kurpaska. **Contributors** - Marcin Kowal, Józef Rzempołuch, Yunok Craze-Romero, George Maddison.

For the Lead Beneficiary	Reviewed by Work package Leader	Approved by Coordinator
Udisien Woy	**Jana Kalivodova**	**Boris Kvizda**

Start date of project: **01/10/2020** Duration: **48 Months**
Project Coordinator Organisation: **VUJE, a. s.** VERSION: 1.1

Project co-funded by the European Commission under the Euratom Research and Training Programme on Nuclear Energy within the Horizon 2020 Programme		
Dissemination Level		
PU	Public	**X**
RE	Restricted to a group specified by the Beneficiaries of the SafeG project	
CO	Confidential, only for Beneficiaries of the SafeG project	

Version control table

Version number	Date of issue	Author(s)	Brief description of changes made
1.0	28/06/2024	See above	First draft
1.1	28/06/2024	M. Velckova S. Bebjak	Review by MST Final version

Project information

Project full title:	Safety of GFR through innovative materials, technologies and processes
Acronym:	SafeG
Funding scheme:	Research and innovation action
ECGA number:	945041
Programme and call	Horizon 2020 Framework Programme for Research and Innovation (2014-2020) NFRP-2019-2020 (Nuclear Fission and Radiation Protection Research)
Coordinator:	Dr. Boris Kvizda
EC Project Officer:	Cristina Fernandez Ramos
Start date – End date:	01/10/20 – 30/09/2024 i.e. 48 months
Coordinator contact:	+421 33 599 1173, Boris.Kvizda@vuje.sk
Administrative contact:	+420 602 771 784, jakub.heller@evalion.cz
Online contacts (website):	www.safeg.eu

„This project has received funding from the Euratom research and training programme 2019-2020 under grant agreement No 945041".

EXECUTIVE SUMMARY

This document aligns with the general proposition for SafeG WP2: *Innovative Materials and Technologies for Enhancing Safety of Gas-cooled Fast Reactors (GFRs)*. It is about the introduction of innovative processes, materials, and technologies into the design of GFRs, particularly the GFR demonstrator ALLEGRO. This deliverable includes work completed as part of Task T2.3, and specifically focuses on advanced manufacturing processes and materials. The purpose was to determine how advanced manufacturing processes may facilitate the manufacturing of selected materials designated for safety critical components. The primary aim was to assess the suitability of these processes for the design and construction of GFRs, and for implementation in the ALLEGRO GFR system.

The selected candidate materials included high-temperature steels, Nickel-based alloys, and metal-ceramics composites. Distinct material development approaches were implemented for FeCrAl-ODS and Inconel 617 alloys, which were selected for processing using powder metallurgy and additive manufacturing techniques. For FeCrAl-ODS alloys, the emphasis was on achieving an appropriate material formulation, while the investigative focus for alloy 617 was on developing the material processing strategy. The overarching goals were to assess the resulting materials and support manufacturing feasibility assessment studies, based on the functional and operational requirements for GFRs.

This foundational work demonstrates the feasibility of adopting advanced materials and processes for Generation IV reactor applications, including GFRs. FeCrAl-ODS alloy formulations were successfully processed to obtain material samples for characterisation. A range of additive manufacturing capabilities were also implemented to demonstrate the viability of selected processing technologies. The initial results demonstrate the potential of these materials and processes for satisfying the design and construction requirements for GFRs. However, further investigation is necessary to incrementally improve promising developments. Future research and development considerations include the refinement, optimisation, validation and scaling-up of experiments, involving both FeCrAl-ODS and Inconel 617 alloys, in accordance with ALLEGRO requirements.

CONTENTS

List of abbreviations

AW	Arc Wire
bcc	Body Centred Cubic
BPR	Ball-to-Powder Ratio
BSE	Selected Backscattered Electron
DED	Directed Energy Deposition
DHR	Decay Heat Removal
DoC	Depth of Cut
DoE	Design of Experiments
EDS	Energy-Dispersive X-Ray Spectroscopy
FC	Furnace Cooled
FIB	Focused Ion Beam
F-M	Ferritic-Martensitic
GFR	Gas-cooled Fast Reactor
GI-XRD	Grazing Incidence X-Ray Diffraction
GMAW	Gas Metal Arc Welding
GTAW	Gas Tungsten Arc Welding
HE	Hot Extrusion
HIP	Hot Isostatic Pressing
HPSC	High Pressure Soluble Coolant
HT	High Temperature
HTBR	High-Temperature Brittleness Range
HTGR	High-Temperature Gas-Cooled Reactor
HTR	High Temperature Reactor
HX	Heat Exchanger
LP	Laser Powder
L-PBF	Laser Powder bed Fusion
LW	Laser Wire
MA	Mechanical Alloying
MQL	Minimum Quantity Lubrication
OA	Open Architecture
ODS	Oxide Dispersion-Strengthened
PM	Powder Metallurgy
Ra	Average Roughness
RT	Room Temperature
$scCO_2$	supercritical CO_2
SEM	Scanning Electron Microscopy
SPS	Spark Plasma Sintering
SRIM	Stopping and Range of Ions in Matter
STEM	Scanning Transmission Electron Microscopy
TEM	Transmission Electron Microscopy
WP	Work Package
WQ	Water quenched
XRD	X-Ray Diffraction

List of figures

List of tables

1 INTRODUCTION

1.1 Purpose

The purpose of Work Package 2 (WP2) is to investigate how innovative materials and technologies may enhance the safety of Gas-cooled Fast Reactors (GFRs). Correspondingly, Task T2.3 is crucial to informing decisions on how selected advanced materials and processing technologies may be leveraged to improve the safety of GFRs. These important safety concerns can be addressed by implementing materials with better performance and adopting advanced manufacturing processes (AMPs) to facilitate the manufacture of these materials.

1.2 Objective

The main task objective was to explore the integration of advanced manufacturing processes and experimental designs for manufacturing materials and components. The materials and components identified as critical, were explored in Tasks T2.1 and T2.2. The specific aim of this task was to assess the suitability of advanced materials and processing techniques for the design and construction of GFRs.

1.3 Scope

The main activities for this task primarily involved the development of representative material samples. The samples were used to assess the feasibility of using designated alloys and processing technologies to enhance GFR applications. Accordingly, different research activities were incrementally progressed, and planned experiments were refined as necessary, based on the task objectives, requirements, interpretations, and considerations applicable to investigated alloys and components.

1.4 Relation to other deliverables

This task relies on inputs from related activities across different tasks, particularly T2.1 and T2.2, which together consist of two general phases. These include a clear definition of critical parts (component, scale, geometry, and material properties) to be investigated, and the manufacturing of different materials that can potentially overcome GFR design challenges. The material options and design challenges investigated in T2.3 were facilitated by related activities. These activities included the compilation of candidate materials for crucial GFR components, as part of the work completed in deliverable D2.1 [1], and the specifications for a key GFR component. The Decay Heat Removal (DHR) Heat Exchanger (HX), reported in D2.3 [2], was selected as the key component underpinning this task.

2 METHODOLOGY

2.1 Overall Strategy

In this section, the methodology for the different investigations completed under task T2.3 is described. Primarily, the goal was to facilitate efficient and effective use of manufacturing resources to achieve the objectives outlined in section 1.2. An outcome driven approach was adopted and involved reviewing the list of selected materials and specific requirements, before proceeding with investigations. Advanced materials that can offer significant functional benefits were investigated, and different options were proposed for each of the SafeG applications under consideration. From these options, oxide dispersion–strengthened (ODS) FeCrAl (chrome-ferrum- aluminium) or FeCrAl-ODS, and Inconel 617 (IN617) alloys were selected for further investigation.

The general development approach for the selected alloys is summarised below.

- The pre-processing stage typically involved the acquisition and preparation of the raw or feedstock material;
- The material processing phase involved the design of experiments (DoE) and manufacturing of material samples, using the advanced processing technologies accessible to SafeG partners;
- The post processing of resulting materials, including the heat treatment, and finishing of samples. Important features such as quality, performance, safety, and related procedures, were also considered.

Distinct approaches were also implemented when developing FeCrAl-ODS and Inconel 617 alloys, based on the specific characteristics and intended application for each alloy. The SafeG methodology for developing advanced materials and processes is depicted in Figure 1.

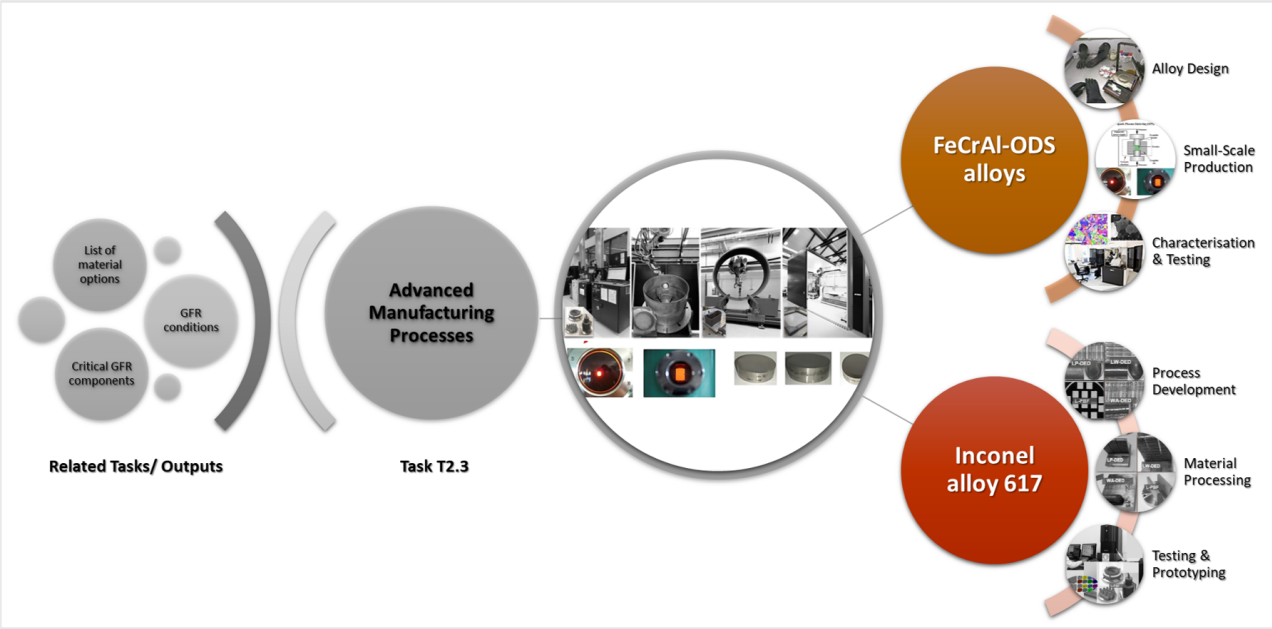

Figure 1:Overall development strategy for selected materials and processes.

The primary empirical objective, when investigating FeCrAl-ODS alloys, was to assess the feasibility of designing an alloy suitable for GRF applications. Experiments involving Inconel alloy 617 were aimed at developing the processing strategy to obtain requisite material samples and components. This distinction was necessary to ensure that each study was appropriately designed in accordance with the SafeG project objectives, and to suit the requirements of ALLEGRO. Furthermore, it provided unique insights into advanced materials and processes, which is consistent with the main purpose of this task.

3 PROCESSING OF FeCrAl-ODS ALLOYS

3.1 Material and processing requirements

This section is about the production and testing of FeCrAl-ODS alloys. The aim was to assess the feasibility of producing FeCrAl-ODS alloys using powder metallurgy methods. In particular, the mechanical alloying and the spark plasma sintering (SPS) methods were considered. The physicochemical and mechanical properties of the FeCrAl-ODS alloys obtained, both at room temperature, and at temperatures within the typical operating range of gas-cooled reactors, were analysed. The investigation also involved evaluating the effects of the addition of Y_2O_3 oxide particles and Ti and V alloying additives on the homogeneity of the microstructure, mechanical properties, and radiation resistance of FeCrAl-based ODS alloys. In summary, the purpose of this work was to investigate the possibility of obtaining FeCrAl-ODS alloys with Y_2O_3, Ti, and V by powder metallurgy techniques, through mechanical alloying (MA), followed by SPS consolidation. The results obtained provided valuable material data, within the context of the preparation and properties of FeCrAl-ODS alloys and their applications in GFRs, particularly the ALLEGRO reactor. Although the results are preliminary, the research team plans to continue attempts to manufacture components from FeCrAl-ODS alloys that can be used in the nuclear industry.

The continued growth in the demand for electricity and industrial heat worldwide is facilitating new nuclear reactor developments and modern energy generation technologies. The need for enhanced efficiency in the operation of nuclear power plants requires improvements in the efficiency of both the reactor and energy conversion systems. Consequently, modern structural materials that satisfy the lifetime durability and environmental performance requirements (high temperature and increased irradiation for at least 60 years) during plant operation are highly desirable. The operating temperatures of Generation IV reactors, including GFRs, range from 500 – 1000 °C, with a maximum radiation damage of about 200 dpa. Thus, it is essential to develop novel advanced materials suitable for nuclear power generation. Among the many promising materials for nuclear power applications are ferritic FeCrAl alloys with different Cr and Al contents [3–6]. FeCrAl alloys are of increasing interest in applications, such as accident-resistant fuel cladding, structural components for fast fission reactors, and as first wall and jacket structures for fusion reactors [7]. A common feature of these components is their utilisation in very harsh environments. As previously mentioned, the materials from which these components are built must show excellent corrosion & radiation resistance in these environments and exhibit high mechanical strength over a high temperature range. Additionally, traditional stainless steels, such as grades 310S or 316L, are unsuitable for use because they are prone to the formation of volatile chromium compounds at high temperatures. Alternatively, an iron-based alloy that forms aluminium oxide, called FeCrAl, can be used [8]. These alloys exhibit improved oxidation and corrosion resistance than FeCr alloys, due in part to their high mechanical strength at high temperatures, and the formation and growth of passive chromium-aluminium oxide (α-Al_2O_3) layers on the surface during high-temperature operation.

These alloys also show good resistance to stress corrosion cracking and resistance to radiation-induced swelling. However, limitations in these alloys include the occurrence of a brittleness effect at 475 °C, (an effect in Fe-based alloys containing high amounts of Cr, usually above 12 wt.%, due to the separation of α and α' phases and in the separation of the σ phase during slow cooling from the operating temperature). Nevertheless, alloys with lower Cr content appear less susceptible to aging embrittlement [9]. Moreover, with regard to the effect of aging embrittlement, the role of the Al additive is often considered, a higher amount (above 5 wt.%) of which may reduce the tendency of the material to separate the α-α' phases, while a lower content of Al may increase that effect [10,11]. A supplementary effect of Al addition is the stabilisation of ferrite in Fe-based alloys with a Cr content of less than 12 wt.% [12]. FeCrAl alloys also exhibit degradation in yield strength and ultimate tensile strength above 1000 °C. Therefore, to improve mechanical properties, mainly creep resistance and yield strength, while improving high-temperature corrosion resistance, an excellent solution could be to reinforce the alloy matrix with oxide particles and highly carbide-forming elements [13]. For this reason, the proposal of

this study is to enrich the developed FeCrAl-based alloys with Ti and V (maximum 1 and 0.5 wt.%) and Y_2O_3 oxide particles. These metallic elements are also well known to be responsible for the reinforcement and improvement of their corrosion resistance in the microstructure of ODS/F-M (ferritic-martensitic) steels, including EUROFER-ODS.

Oxide dispersion-strengthened steels and alloys (ODS) have been studied for many years, focusing on their fabrication processes, mechanical strength, and different chemical compositions. Alloying elements in these materials, such as Al, W, Ti, Ta, V, Zr and Y_2O_3 oxides, are often added to improve the properties and stability of the original solid solution matrix, and to form complex oxides and carbides, before and during operation. The most commonly formed non-stoichiometric complex oxide nanoparticles and nanoclusters are Y-Al-O, Y-Ti-O, Y-Zr-O, or, less commonly, Ti-W-O. Due to these additions, ODS alloys present many exceptional properties, such as high radiation resistance, good mechanical properties, creep resistance and a low activation effect, which is essential for nuclear applications [14–16]. However, FeCrAl-ODS alloys are studied less extensively than pure FeCrAl alloys. Consequently, a paucity of available literature on FeCrAl-ODS alloys is a motivating factor for the investigation of these alloys and their manufacturing.

The primary aim of the NCBJ research team was to manufacture model FeCrAl-ODS alloys with Ti and V additions. Accordingly, eight FeCrAl-ODS alloy compositions were prepared, as presented in Table 1.

Table 1: Chemical composition of powders used for manufacturing of FeCrAl-ODS alloys.

Sample Description	Chemical composition [wt.%]					
	Fe	Cr	Al	Y_2O_3	Ti	V
M1	Balance	9.0	5.0	0.3	0.5	-
M2	Balance	9.0	5.0	0.3	1.0	-
M3	Balance	12.0	5.0	0.3	0.5	-
M4	Balance	12.0	5.0	0.3	1.0	-
M5	Balance	9.0	5.0	0.3	0.5	0.5
M6	Balance	9.0	5.0	0.3	1.0	0.5
M7	Balance	12.0	5.0	0.3	0.5	0.5
M8	Balance	12.0	5.0	0.3	1.0	0.5

Iron is the base element in all manufactured ODS alloys. The Al content was fixed at 5 wt.%, while the content of Y_2O_3 was fixed at 0.3 wt.% in all the investigated samples. As mentioned previously, aluminium improves oxidation resistance by forming a protective oxide layer on the surface during operation at high temperatures. Y_2O_3 oxide was especially selected as a strengthening phase because it exhibits a high melting point, high chemical stability, and low solubility with the metal matrix. The addition of yttrium oxide can also have a significant effect on the aging brittleness at elevated temperatures close to the operating temperatures of generation IV reactors. The amount of Al and Y_2O_3 was selected based on data from literature and insights from the authors' experience of testing F/M-ODS alloys [17–20]. Literature studies indicate that the presence of nanoscale oxide particles in ODS steels reduces the aging brittleness. The content of Cr, which is a ferrite stabilizer, is either 9 or 12 wt.% in the samples. However, slight differences in Cr or Al could significantly impact the "475 °C embrittlement" effect related to the alpha and alpha prime phase separation. Moreover, very fine, densely dispersed oxide particles can hinder or delay the formation of the chromium-enriched alpha phase by influencing the chromium diffusion pathway in the matrix. Kobayashi et al. studied the effects of varying Cr and Al contents on FeCrAl alloys and reported that the addition of Al can suppress the "475 °C embrittlement" in the FeCrAl alloys containing more than 12 wt.% of Cr. The studies of FeCrAl alloys by Han et al. also indicate that appropriately balancing Cr and Al content can limit "475 °C embrittlement" [21,22]. Based on this data and analysis of the Fe-Cr-Al phase diagrams, the authors also planned to focus on resistance to "475 °C embrittlement". The experimental results are shown in detail

later in this report. The content of Ti in the samples is either 0.5 or 1 wt.%. The small addition of Ti can improve the corrosion resistance of the alloys, which will be studied later in detail. Moreover, the high affinity of Ti toward oxygen could lead to the formation of complex nanometric oxide precipitates. Considering the effects of Ti addition, in the first phase, alloy samples were produced only with Ti addition. In the subsequent phase, the alloy samples were modified by adding vanadium to their composition in a volume not exceeding 0.5 wt.%. Such a small amount of V (0.5 wt.%) was added to the selected samples to enhance the effect of forming nanometric oxide precipitates. Nevertheless, it should also be noted that vanadium has a high affinity for carbon, which results in carbide phase formation. Therefore, it was rationalised that the inclusion of Ti and V, to the alloy compositions considered in this study, could improve the mechanical properties and microstructure stability in creep and radiation conditions.

3.2 Fabrication and testing

The most common technique used to produce ODS metallic alloys is powder metallurgy (PM) [23–26], which involves the MA of powders, followed by densification of the material by sintering (mostly at high temperatures). The use of sintering under pressure allows for the manufacture of materials with very high density, low porosity and good mechanical properties. Raw metallic elements and oxide powders (e.g. Y_2O_3) are ground together in a high-energy milling process to produce a relatively homogeneous powder mixture with limited agglomerates. As a solid-state technique, MA has many advantages over liquid methods, such as increased solubility of the elements, absence of segregation of the casting and absence of issues with significantly different melting temperatures when producing alloys consisting of multiple chemical elements [25]. However, the most prominent advantage of MA is the production of a powder with an ultra-fine-grained morphology (i.e., taking the full potential of the Hall-Petch effect), which is known to have a positive effect on the mechanical properties and structure of the bulk material.

The powder formed during the MA method is then consolidated. During sintering, complex oxides precipitate from oxide particles (e.g., Y_2O_3), homogenously distributed during mechanical alloying, and form a stable matrix (i.e., with high affinity for oxygen elements, such as Al, Ti etc). In literature, the most commonly used methods for the consolidation of ODS alloy powders are hot isostatic pressing (HIP), hot extrusion (HE), and SPS. Although SPS is applied less extensively to bulk ODS alloys than HIP and HE, there is growing interest in this technique [27].

Compared to other methods, SPS has some positive features. Firstly, short-term heating in the SPS method allows almost complete compaction and production of complex compositions with nano-size oxides, which promotes high mechanical and creep resistance properties. The second advantage is that using this method prevents coarse-graining of nanoparticles and excessive grain growth, enabling the preparation of bulk samples with matrix grain sizes typically below 1 μm [28]. The sintering speed is a third advantage of the SPS process, as there is no loss in ambient heating, and the energy is supplied strictly to the sintered material by means of high-current DC pulses. The energy supplied to the powder consolidated in the matrix is much higher than that of other methods. Therefore, it is possible to carry out the sintering process at temperatures up to 30% lower than the standard methods mentioned. Nevertheless, there are also some disadvantages. The most critical is that short-term sintering does not allow significant diffusion to homogenize the materials, which is a critical point to obtain assumed properties [29]. Accordingly, it should be noted that thermo-mechanical treatment, such as application of hot rolling or controlled heat treatment procedures after sintering, can significantly affect the properties of ODS alloys [30–32].

A general roadmap for the preparation, manufacturing, and testing of the FeCrAl-ODS alloys, is presented in Figure 2.

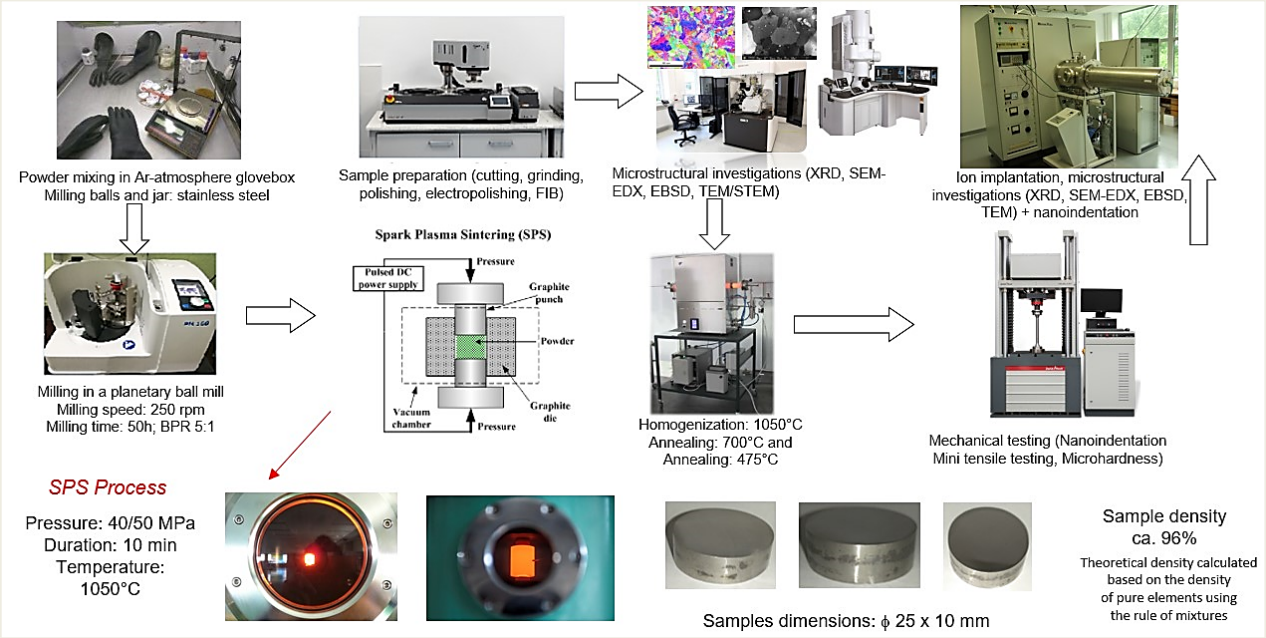

Figure 2: FeCrAl-ODS alloys preparation, manufacturing, and testing roadmap.

3.2.1 Powder preparation

Manufacturing and investigation of FeCrAl-ODS alloys started with the acquisition and preparation of the powders for MA. Prior to MA, all powder-processing procedures were conducted in a laboratory glove box, under an inert argon atmosphere. Pure alloy constituent powders had an initial particle size of less than 150 microns. The purity and particle size of the commercially acquired powders, from ALFA AESAR Thermo Fisher Scientific, are listed in Table 2.

Table 2: Purity and particle size of commercial powders (ALFA AESAR Thermo Fisher Scientific) used for manufacturing of the FeCrAl-Y_2O_3-Ti-V ODS alloys

Component	Fe	Cr	Al	Y_2O_3	Ti	V
Purity	99.9% metal basis, C ≤ 0.2%, O ≤ 0.4%	99.99% metal basis, C < 10 ppm, O < 160 ppm	99.5% metal basis	99.9%, total rare earth oxide 0.1% max.	99.8% metal basis, C = 0.086%, O = 0.694%	99.5% metal basis, C ≤ 0.034% O ≤ 0.035%
Particle size	< 20 µm	<150 µm	< 30 µm	< 10 µm	< 70 µm	< 40 µm

The procured powders were combined, to obtain a homogenous granular mixture. The MA process was carried out in a Retsch PM100 planetary ball mill. Each milling batch yielded about 50 g of powder. In order to maintain the cleanliness of the alloy's composition after each grinding process, the container and balls were cleaned with quartz sand, washed with ethanol in an ultrasonic cleaner, and dried in a laboratory dryer. The same cleaning procedure was implemented for the grinding container, to remove any residual elements from the previous compositions. The balls and grinding jar material are made from X90CrMoV18 martensitic stainless steel. One hundred and eighty-five Ø7 mm balls were used, giving a ball-to-powder ratio (BPR) ratio of 5.18, relative to the weight of the ground powder. The mechanical alloying duration was about 50 hours at 250 rpm, with a 15-minute break applied every 15 minutes, to ensure the mechanical alloying process was maintained at, or close to room temperature (RT). The MA procedure was performed without the addition of a process control agent. Before the grinding process, one gram of powder was taken from each batch for x-ray diffraction (XRD) and

scanning electron microscopy (SEM) tests. This step was necessary to facilitate comparisons between the morphology and size of the powder particles, before and after the mechanical synthesis process.

3.2.2 Spark plasma sintering (SPS)

The mechanically alloyed powders were consolidated using the SPS technique, in a device designed by the Lukasiewicz Institute of Microelectronics and Photonics (Warsaw, Poland). The aim of using the SPS technique was to preserve the microstructure of the starting material as much as possible. It was also done to protect the grains from excessive growth, which is possible for a short time during the SPS process, when the material is subjected to high heating and cooling rates. The choice of the SPS method was dictated by the possibility of sintering powders with very high melting points, such as yttrium oxide, the melting point of which is 2425 °C. The SPS process was conducted in a graphite round die, with a diameter of 25 mm, and at a heating rate of 100 °C/min up to 900 °C. After reaching 900 °C, the heating rate was lowered to 50 °C/min until the sintering temperature level of 1050 °C was achieved. The sintering temperature and uniaxial pressure of 40 MPa were maintained for 10 minutes before the samples were slowly cooled down, at an average cooling rate of 10 °C/min. After the sintering process, a homogenization annealing process was performed at 1020°C for 30 minutes, under an argon atmosphere, before cooling the samples in the air.

3.2.3 Material characterisation

The investigation of the properties of FeCrAl-ODS alloys commenced with analyses of powders. The raw powders were investigated, before and after the MA process. A scanning electron microscope (SEM) equipped with energy dispersive X-ray spectroscopy (EDS) was used to evaluate the average size of powder particles, the homogeneity of alloyed powders, and the chemical composition. Microscopic analyses of the powders were also performed, using a Zeiss EVO MA10 SEM and a Thermo Fisher Scientific™ Helios™ 5 UX scanning electron microscope. The evaluation of the phase structure and crystallite size of raw and mechanically alloyed powders were performed using X-ray diffraction (XRD) techniques, and a Bruker D8 Advance diffractometer. The resulting data was analysed using a Bruker DIFFRAC.EVA and a DIFFRAC.TOPAS software. The same devices were also used to perform XRD analyses on bulk or processed material samples.

The density of the bulk FeCrAl-ODS material samples were analysed after the SPS and homogenization annealing procedures. The density was measured according to Archimedes' principle. Before measurements, samples were polished using SiC abrasive papers (approximately 0.5 mm), to limit the effect of surface contamination by carbon from the graphite die or oxidisation during heat treatment. The density measurements were performed by weighing the samples in air and distilled water at 23 °C. The measured densities were then compared with the theoretical densities calculated, based on the rule of mixtures, using pure element densities. Next, the chemical composition of bulk samples was measured precisely using X-ray fluorescence (XRF) spectroscopy and SEM-EDS techniques. However, oxygen and carbon are crucial in forming nanometric oxide and carbide precipitates in ODS alloys, and the precision of the measurements of light elements obtained using SEM-EDS is very limited. Therefore, the measurements of oxygen and carbon content in the bulk samples were performed using LECO CS-600 and TCHEN600 devices.

The microstructure of bulk FeCrAl-ODS material samples were characterised. SEM-EDS and electron backscatter diffraction (EBSD) analyses were carried out using a Thermo Fisher Scientific™ Helios™ 5 UX SEM. The samples for these techniques were prepared first by mechanical polishing using SiC abrasive papers up to P1200 grit. Then, the samples were electropolished in 60% perchloric acid (70 ml) and ethanol (1000 ml) under the voltage of 30 V for a duration of 50 s at 10°C, using a LectroPol-5 device by Struers. The SEM and EBSD investigations were aimed at characterising the microstructure of bulk samples, in terms of grain size, precipitate distribution, and chemical composition. The grain analysis of the collected EBSD data was conducted using EDAX OIM Analysis 8 software. Moreover, for

the purpose of better characterisation of nanometric precipitates (size distribution, volume fraction, chemical composition, etc.), transmission electron microscopy (TEM) investigations were carried out using a JEOL JEM 1200EX II TEM and a JEOL JEM-F200 with EDS detector. The lamellae for TEM characterisations were prepared using the focused ion beam (FIB) technique. The total area of images used for the calculations was approximately 5 μm^2. Based on scanning TEM (STEM) and TEM images, the size distribution and particle volume fraction analysis were determined using ImageJ software.

The mechanical properties were measured using different techniques, including nanoindentation, Vickers hardness measurements, and tensile tests. The nanoindentation measurements were carried out using a NanoTest Vantage System by Micro Materials Ltd. at ambient temperature with a Berkovich-shaped diamond indenter tip. The nanoindentation tests were conducted in a single-force mode by applying eleven different forces ranging from 0.5 to 10 mN. The measurements were repeated at each load twenty times, with a 20 µm spacing between indentations. The dwell time was fixed at 2 s. Loading and unloading times were set at 5 s and 3 s for lower loads (0.5–4 mN) and 10 s and 5 s, respectively, for higher loads (5–10 mN). The nanoindentation data was analysed based on the load–displacement curves by applying the Oliver and Pharr method. The Vickers microhardness measurements were performed with a force of 4.90 N using a DuraVision device by Zwick/Roell. For each sample, ten measurements were performed after SPS and homogenization annealing. The tensile tests were performed on miniaturised samples using a Z020 AllroundLine testing machine by Zwick/Roell. The physical dimensions of miniaturised tensile specimen are shown in Figure 3.

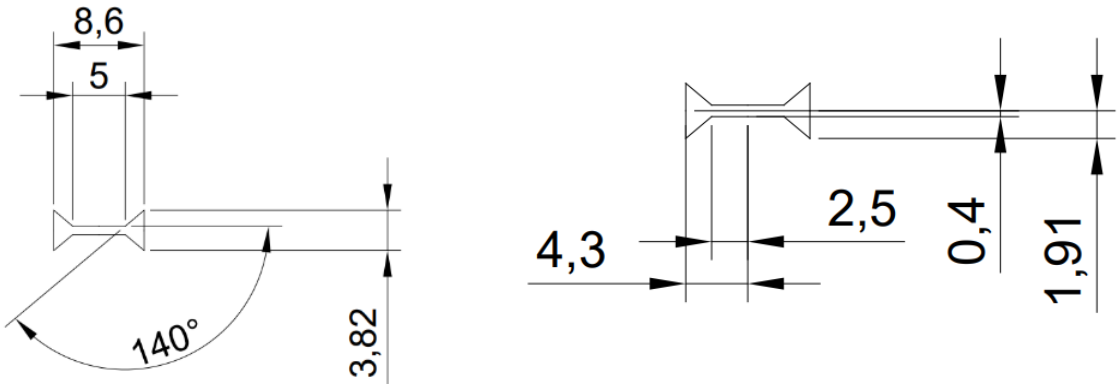

Figure 3: The dimensions of the miniaturised specimen.

As previously indicated, different heat treatments were carried out to evaluate changes in the microstructure and mechanical properties of FeCrAl-ODS samples. Firstly, a homogenization annealing procedure was performed at 1020°C for 30 minutes under an argon atmosphere, followed by a cooling procedure outside the furnace, in air. The investigations by SEM, TEM, XRD, and some mechanical tests were performed on the samples after homogenization annealing. The samples were also annealed at 475°C for 1000 hours, to evaluate the susceptibility of the FeCrAl-ODS alloys to embrittlement (so-called "475°C embrittlement").

Finally, the ion irradiation resistance of selected FeCrAl-ODS alloys was also investigated. The samples were ion irradiated with Fe^{2+} ions of 10 MeV energy up to 5 dpa at 300°C. The irradiated samples were characterised using nanoindentation, Grazing Incidence X-Ray Diffraction (GI-XRD), and TEM techniques. The analytical aim was to support a critical assessment of the potential application of the studied FeCrAl-ODS alloys for components (claddings) of Generation IV reactors.

3.3 Results and analysis

Firstly, the investigations of commercially procured elemental powders for the purpose of mechanical alloying (see section 3.2.1), were conducted by SEM. The images of raw powders reveal significant differences in the morphology and size of powder particles, as shown in Figure 4.

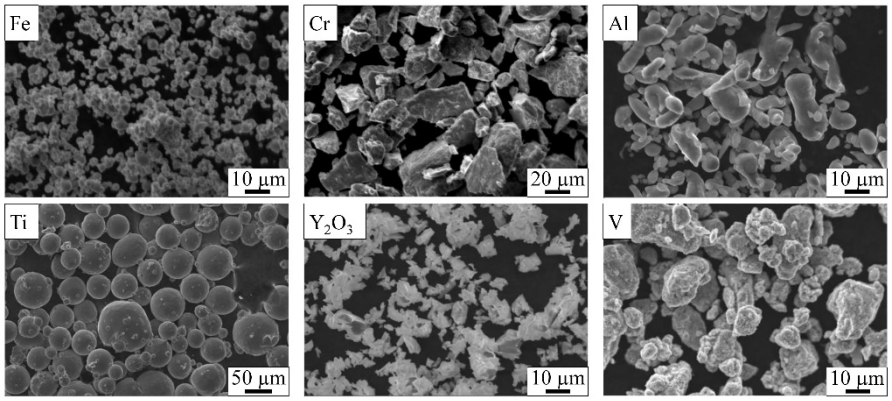

Figure 4: SEM images of raw powders used for the mechanical alloying of FeCrAl-ODS alloys compositions.

The mechanically alloyed powders present significantly different morphology than the raw elemental powders. However, small differences in the chemical composition of alloyed powders do not result in significant morphological changes between them. The SEM images of selected mechanically alloyed powders are shown in Figure 5. The particle size varies significantly for each sample. Specifically, there are many small particles of a few micrometres, but also large agglomerates of 150 µm. The average particle size is approximately 50 µm. The SEM-EDS chemical composition analyses, presented in Figure 5, reveal a homogeneous distribution of elements in all powder particles.

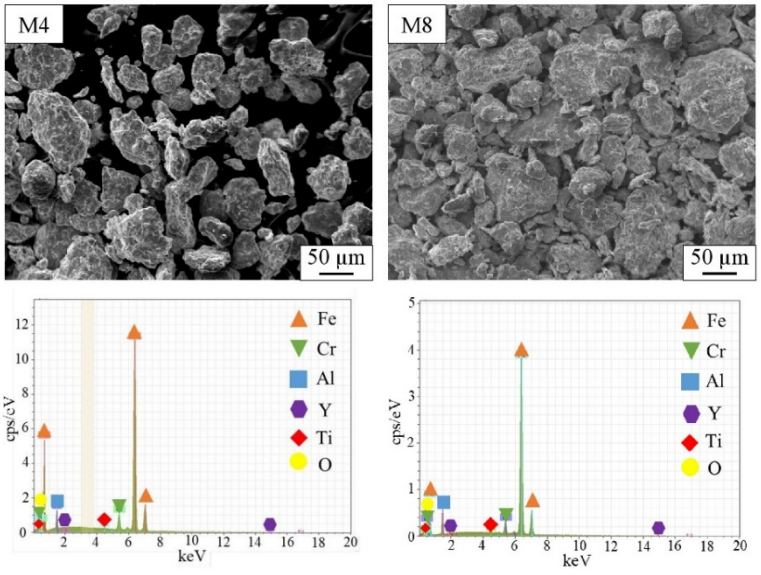

Figure 5: SEM images and EDS spectra of selected powders.

The XRD analyses (Figure 6) reveal that the mechanically alloyed powders of FeCrAl-ODS consist of two body centred cubic (bcc) phases with lattice parameters close to each other. The investigations show a decrease in crystallite size during mechanical alloying, which was expected to undergo deformation during powder milling. The crystallite size of iron powder before MA is 74 nm, while the crystallite size of the mechanically alloyed powder is approximately 25 nm.

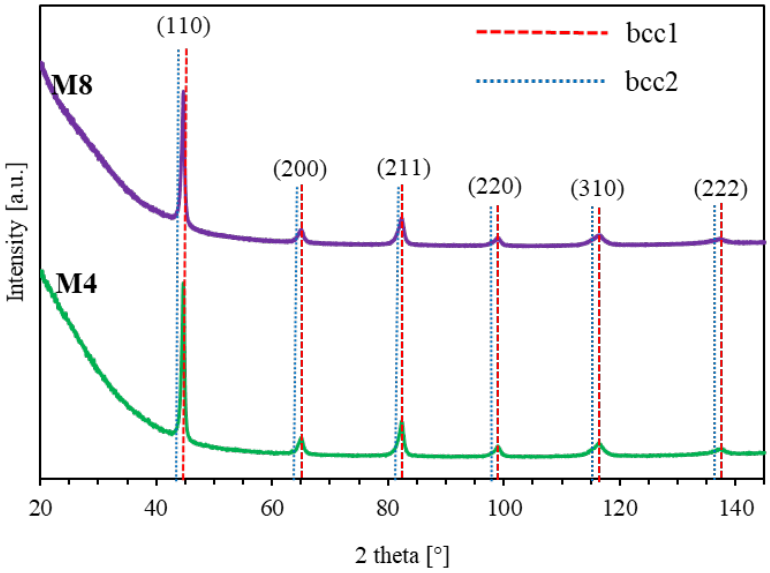

Figure 6: XRD pattern of selected mechanically alloyed FeCrAl-ODS powders.

The mechanically alloyed powders were consolidated using the SPS technique. The macroscopic image of the produced bulk samples with a diameter of 25 mm is shown in Figure 7. The samples show good densification with a relative density between 94.5 and 96.1%. The XRF chemical composition measurements reveal that the composition of each sample is close to the initial composition of the mixture of powders.

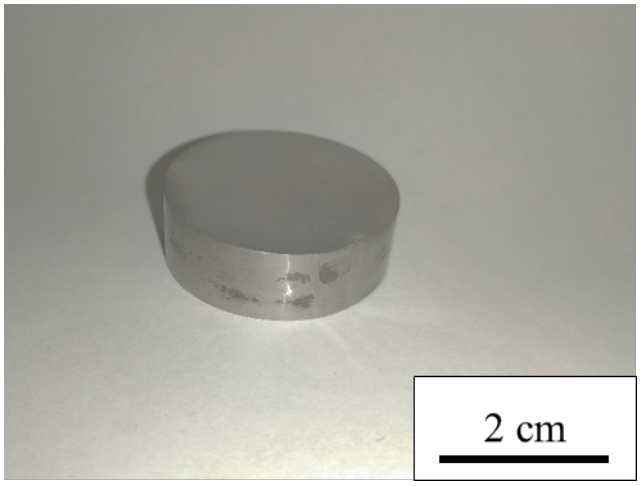

Figure 7: Macroscopic image of FeCrAl-ODS bulk sintered sample.

The XRD analyses of bulk samples reveal the presence of a single bcc matrix phase in all studied samples. The results show a significant change compared with the mechanically alloyed powders, which revealed two bcc phases. Therefore, the sintering led not only to the consolidation of powder into the bulk samples but also to further homogenization, leading to the formation of a single bcc phase. The XRD patterns of selected bulk samples are shown in Figure 8. The lattice parameter of the bcc phase varies slightly depending on the chemical composition of the sample. It should be noted that only peaks of the bcc phase are present. However, the nanometric oxides and carbides are assumed to be present in the bulk samples. Their presence is not detected by XRD due to their small volume fraction and small size. Further analysis and characterisation studies are necessary to confirm this assumption.

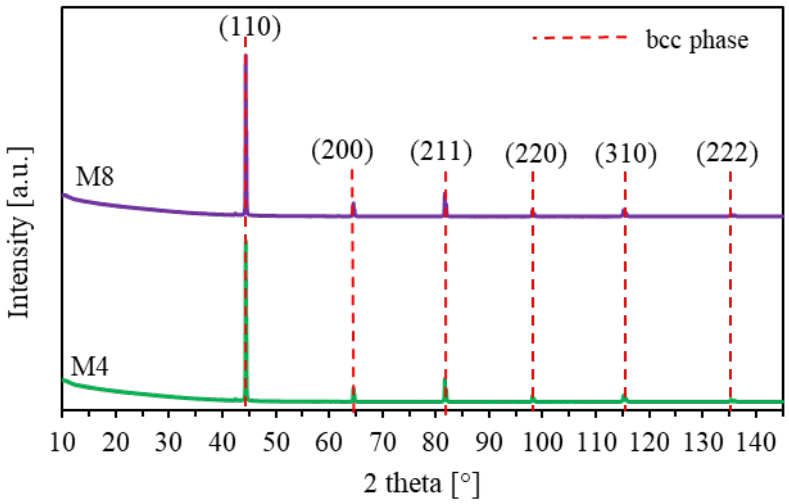

Figure 8: XRD patterns of selected FeCrAl-ODS bulk samples.

The SEM and EDS analyses confirm the results of XRF, revealing the chemical composition close to the initial composition of powders. However, it should be noted that XRF and SEM-EDS are not adequate tools for detecting carbon and oxygen contents. Therefore, analyses using LECO devices were performed to precisely measure the carbon and oxygen contents. The measured carbon content was between 0.030 wt.% and 0.078 wt.%, depending on the sample. Different sources of carbon contamination were considered. One of the sources is the pre-existing carbon content in raw metallic powders that were commercially sourced. The other carbon source could be the milling media (grinding jar or balls) during mechanical alloying. Carbon can also be introduced by diffusion from graphite die during sintering. It should be noted that the presence of carbon could be beneficial in terms of mechanical properties due to the formation of reinforcing carbides. The measured oxygen (using LECO analysers) content was between 0.42 wt.% and 0.44 wt.%. The oxygen content was intentionally introduced via 0.3 wt.% of Y_2O_3 powder to form reinforcing oxide precipitates. However, the excess oxygen content is assumed to be from contamination during the preparation of samples, e.g. during mechanical alloying, despite performing the process under an argon atmosphere and the presence of oxygen in raw metallic powders.

The SEM observations of microstructure, shown in Figure 9, revealed the presence of equiaxed bcc grains. Most of them are in size below 1 µm; however, larger grains up to 8 µm are also present. Many precipitates, significantly below 500 nm in size, are present inside the grains of the matrix phase and at the grain boundaries. The SEM-EDS analyses revealed different areas of enrichment in Al, Ti, or Y, which correspond to various types of small precipitates. The SEM observations confirmed good densification of the samples, without visible indications of significant porosity. The differences in terms of microstructure between samples with different compositions are not very substantial in SEM analyses. However, EBSD analyses reveal that the grain size of the samples containing vanadium is slightly smaller than that of vanadium-free samples. The average grain size of all samples is approximately 1 µm. The selected EBSD maps and the histogram of the grain size are shown in Figure 10. The crystallographic orientation of the grains is totally random – no preferred orientation, which should result in isotropic properties.

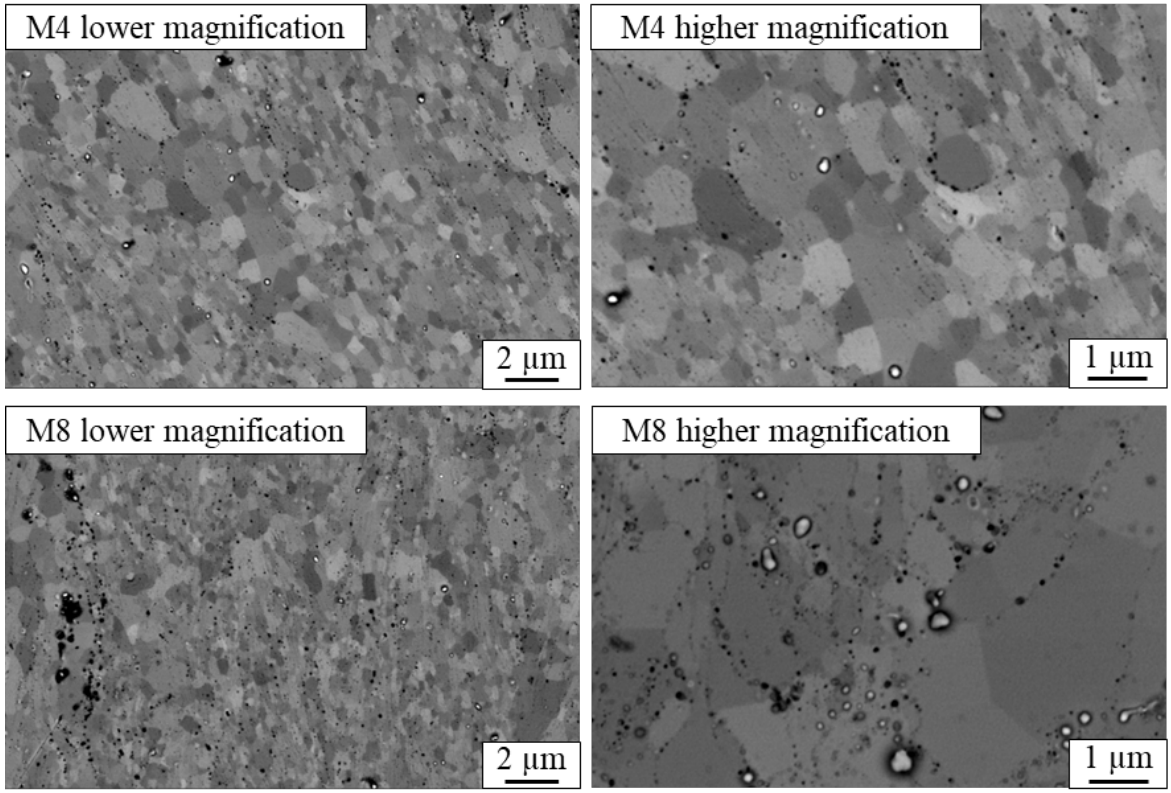

Figure 9: SEM backscattered electron images of microstructure of selected FeCrAl-ODS bulk samples.

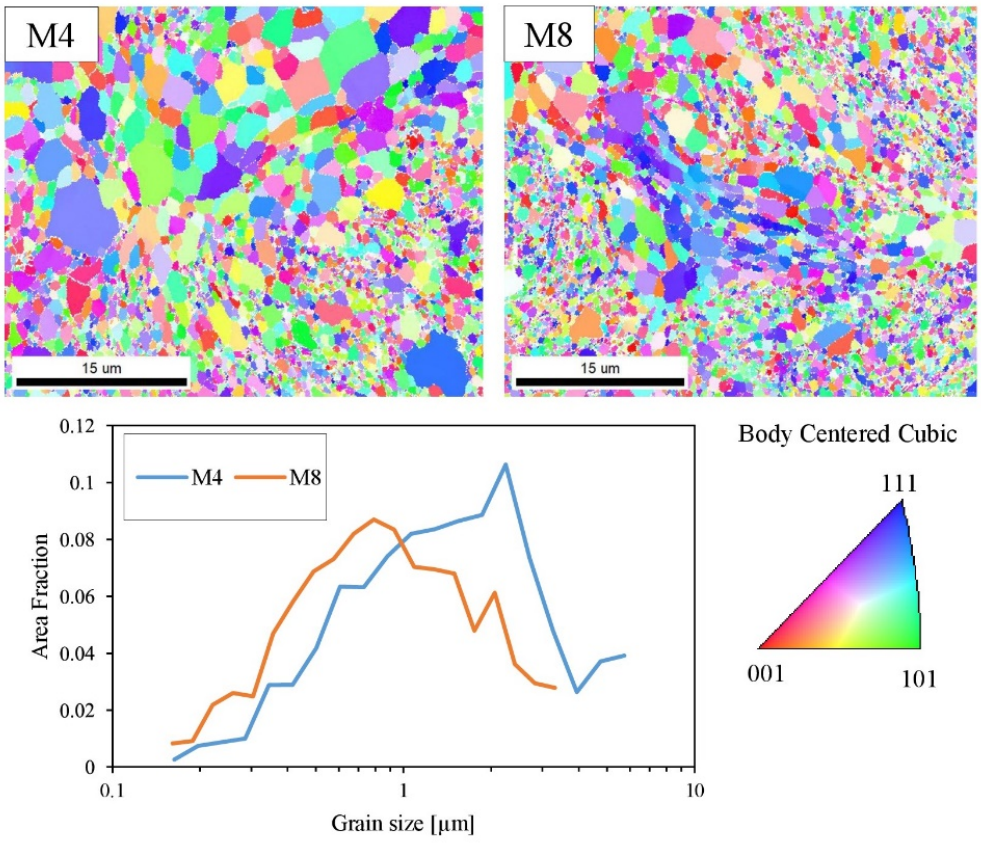

Figure 10: EBSD inverse pole figure maps of selected samples and the histogram of the grain.

The TEM studies were performed to characterise the nanometric precipitates, which are crucial for good mechanical properties and high irradiation resistance. The TEM observations reveal a high-volume fraction of various nanometric precipitates. The selected TEM images and histogram of the size of nanometric precipitates are shown in Figure 11. The volume fraction of the nanometric precipitates is higher in vanadium-containing samples, e.g., in the M8 sample is 2.57%, compared with vanadium-free samples, e.g., in the M4 sample is 1.87%. It shows a positive impact of vanadium on the formation of nanometric precipitates. The observations reveal that a large majority of precipitates are below 50 nm. Such small precipitates can increase strength without causing brittleness and can act as sinks for irradiation-induced defects. The EDS analyses in TEM confirm the presence of various types of nanometric precipitates. The example of STEM elemental EDS elemental maps of M8 samples is shown in Figure 12. Most precipitates are Al-rich oxides. Moreover, there are also oxides rich in Y and V. Nanometric zones rich in carbon, titanium, and vanadium are also present. These precipitates are assumed to be carbides.

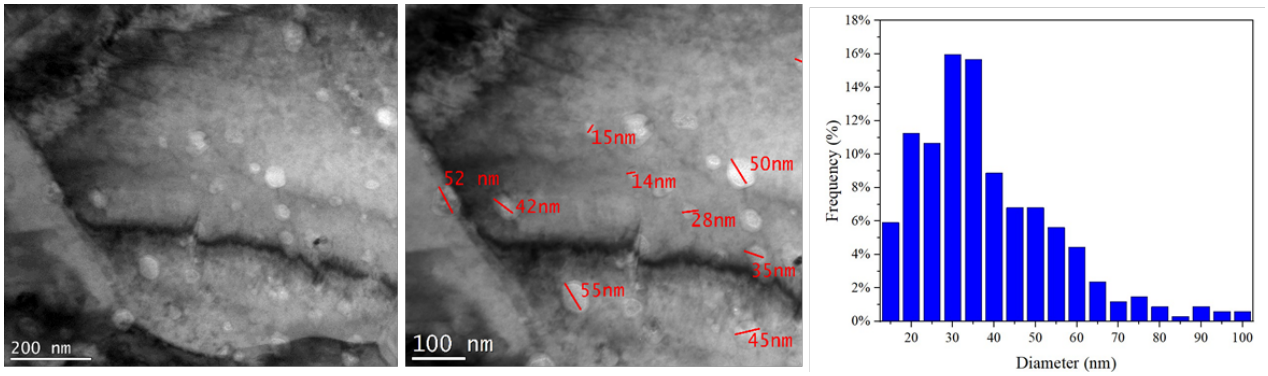

Figure 11: TEM bright field images of the FeCrAl-ODS M8 sample and the histogram of nanometric precipitates size distribution.

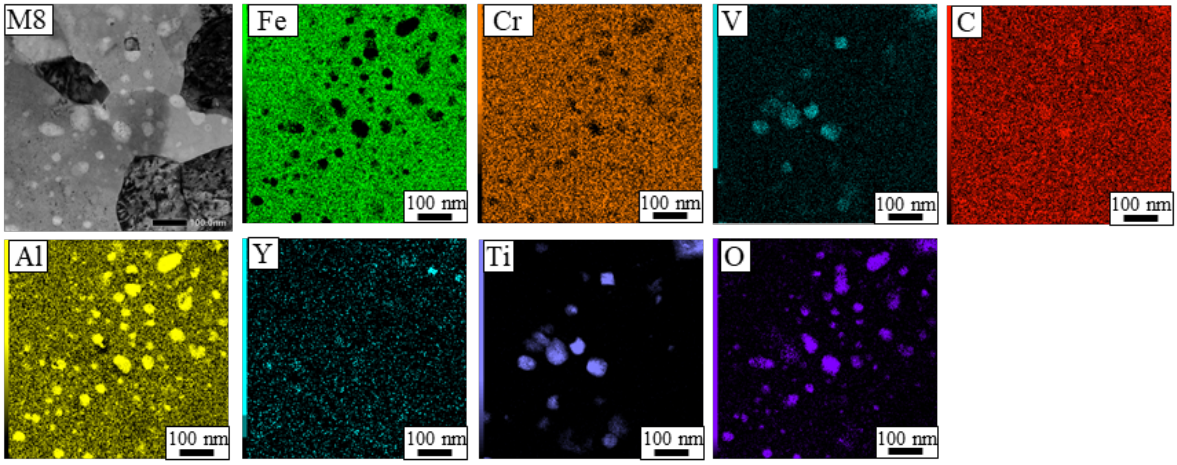

Figure 12: STEM-EDS elemental maps of FeCrAl-ODS M8 sample revealing different nanometric precipitates.

Homogenization annealing was performed at 1020°C for 30 minutes in an argon atmosphere, followed by cooling in air outside the furnace. The objective was to increase the relative density and to evaluate the impact of the heat treatment on the microstructure and properties. The measurements of relative density, shown in Figure 13, indicate a slight increase in the relative density in all studied samples. This is attributed to the closing of some pores during high-temperature treatment.

The XRD, SEM, EBSD, and TEM investigations do not reveal significant changes in the structure and microstructure after homogenization annealing. The XRD results after annealing show a single bcc phase structure with a slightly different lattice parameter than after SPS. The SEM and EBSD analyses reveal only very limited grain growth in all studied samples. The average grain size is still approximately 1 µm.

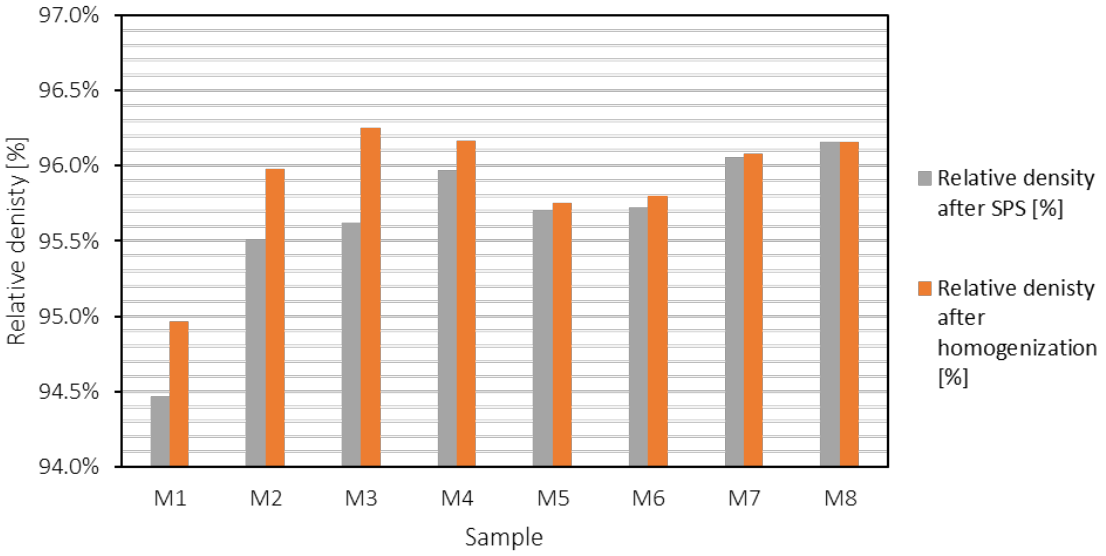

Figure 13: The results of relative density measurements in the FeCrAl-ODS samples after SPS and after homogenization annealing.

However, the TEM investigations (shown in Figure 14) revealed a slight increase in the volume fraction of precipitates in the vanadium-containing samples, for example, 2.57% in the M8 sample after SPS vs. 2.64% in the M8 sample after homogenization annealing. Therefore, it shows that the homogenization annealing could result in the precipitation of additional nanometric precipitates. It should be noted that the size of precipitates before and after annealing is almost the same.

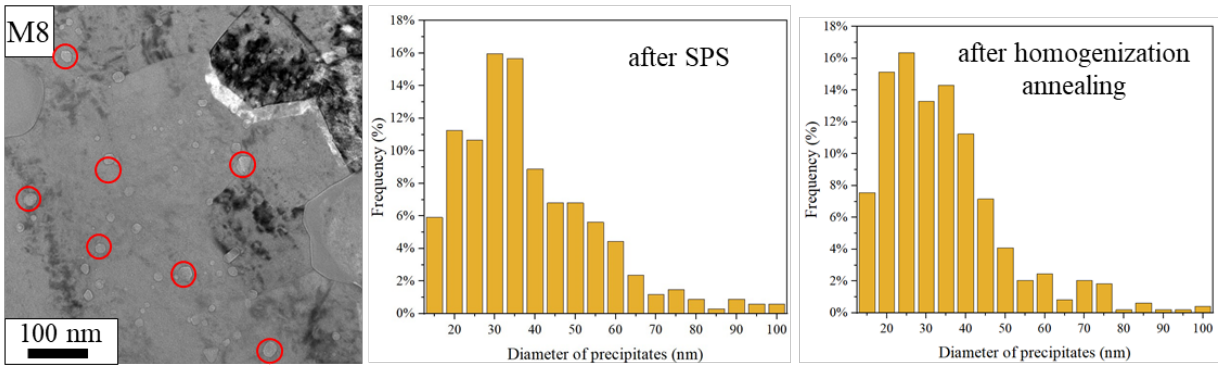

Figure 14: TEM bright field image of FeCrAl-ODS M8 sample after homogenization annealing showing nanometric precipitates and histograms of precipitates size distribution histograms after SPS and after annealing.

The hardness measurements, shown in Figure 15, reveal various hardness values depending on the chemical composition of the samples. The hardness of samples containing vanadium (M5-M8) increases after annealing, while the hardness of vanadium-free samples decreases after annealing (except for the M4 sample). The increase in hardness after annealing is attributed to the formation of additional vanadium-rich precipitates, which was confirmed by TEM investigations.

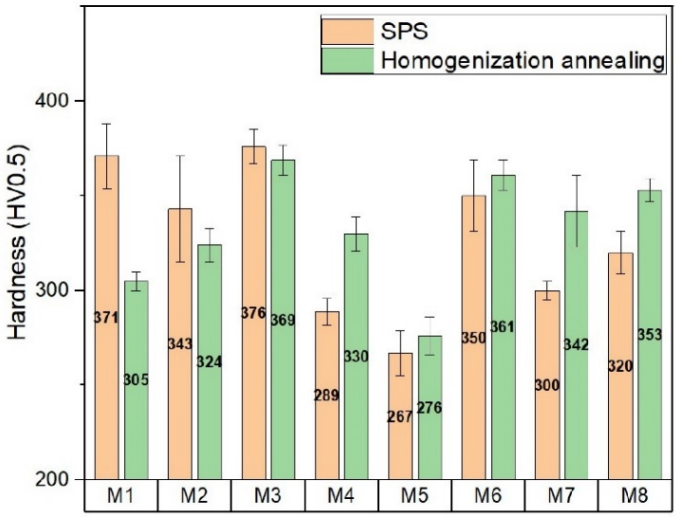

Figure 15: Results of hardness measurements of FeCrAl-ODS samples after SPS and after homogenization annealing.

The mechanical properties of the bulk samples after homogenization annealing were also determined by tensile tests at room temperature using miniaturised samples. The selected stress-strain curves are shown in Figure 15. The tensile test results show very high yield strength ($R_{p0.2}$) of all tested samples, (i.e. between 748 and 896 MPa). The ultimate tensile strength is between 920 and 993 MPa, which is a very high value for FeCrAl-ODS alloys. The elongation at fracture, measured at room temperature is between 11 and 13%, which is somewhat limited for engineering materials. However, it should be noted that these values are comparable with those of other ODS materials produced by powder metallurgy techniques. Samples prepared by the sintering of powder usually show some residual porosity. Even though the samples in this study reveal high relative density, there is still some residual porosity, which can significantly limit the ductility of the material. Moreover, the presence of nanometric oxide and carbide particles (and more importantly slightly large particles of a few hundred nanometres) could also significantly limit the elongation of the material before fracture, because these particles could initiate cracks. Nevertheless, it should be noted that the studied FeCrAl-ODS alloys exhibit very high strength compared to other similar materials.

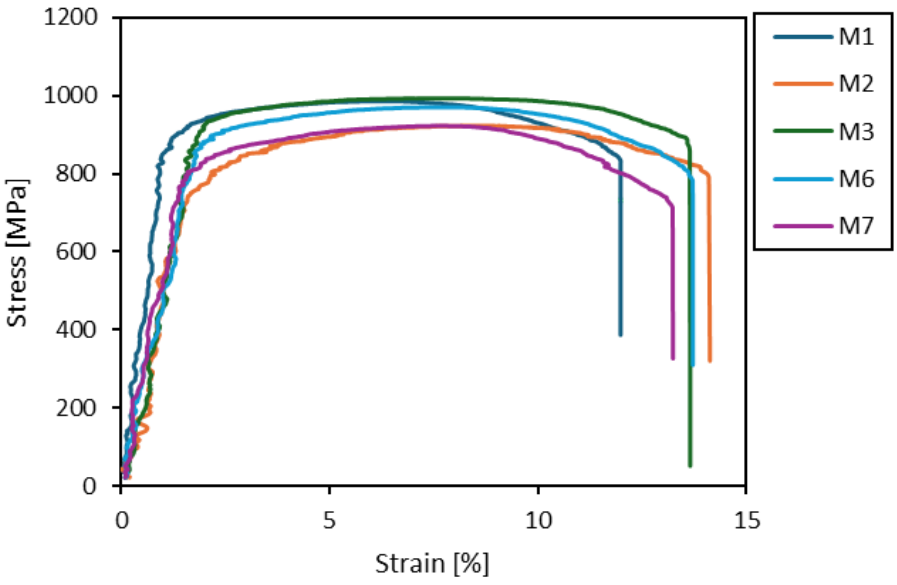

Figure 16: Tensile stress-strain curves of selected FeCrAl-ODS samples acquired at room temperature.

Another phase of the investigation of FeCrAl-ODS alloys concerns the 475°C embrittlement. The "475°C embrittlement" consists of the separation into two bcc phases (α rich in Fe and α' rich in Cr) in single bcc alloys containing Fe and Cr after prolonged exposure to the temperature near 475°C. This phase separation results in a significant increase in hardness and brittleness. Therefore, it should be avoided in materials in all engineering applications. The annealing of the M4 and M8 samples at 475°C for 1000 hours shows the hardness increase in both samples. The results of hardness measurements are shown in Table 3. The increase in hardness for M4 (vanadium-free sample), is slightly more pronounced than in M8 (vanadium-containing sample). It should be noted that the EBSD investigations (not shown here) do not reveal significant changes in the microstructure of the samples. The grain size is similar to the samples after homogenization annealing at 1020°C for 30 min. The tensile test results of the M8 sample after 475°C annealing, which is shown in Figure 17, reveal a slightly higher ultimate tensile strength than the sample before 475°C annealing while the elongation at fracture is comparable to the sample before annealing. Therefore, the brittleness of the M8 sample does not significantly increase after prolonged heat treatment at 475°C. Hence, the produced FeCrAl-ODS samples reveal some resistance to "475°C embrittlement".

Table 3: Hardness of FeCrAl-ODS M4 and M8 samples after different manufacturing and processing conditions.

Sample	Hardness [HV0.5]		
	SPS	Homogenization annealing at 1020°C/30 min	Annealing at 475°C/1000 h
M4	289±7	330±9	345±3
M8	320±11	353±6	363±8

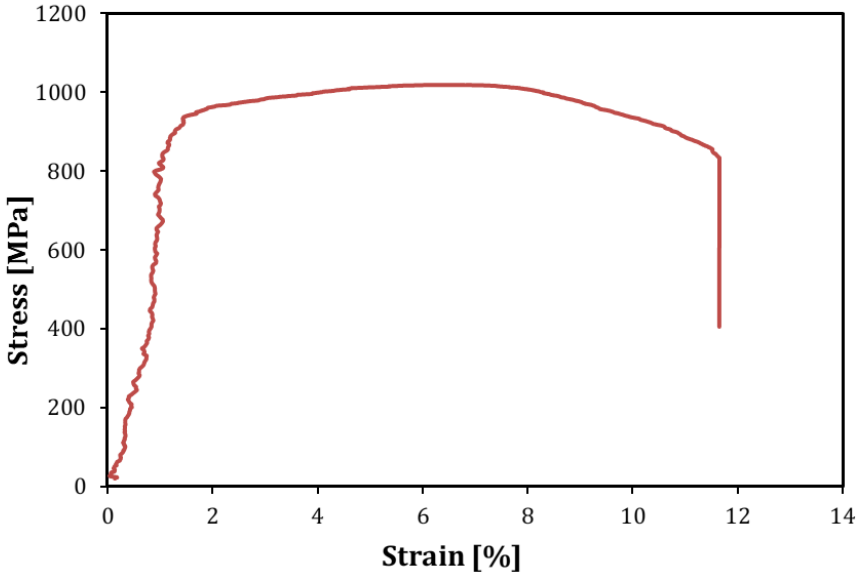

Figure 17: Tensile stress-strain curve of the M8 sample after annealing at 475°C for 1000 h.

The irradiation resistance of FeCrAl-ODS alloys was evaluated by ion-irradiation experiments using Fe^{2+} ions carried out at 300°C. One sample was irradiated up to 1 dpa, and the other sample was irradiated up to 5 dpa. The ion-irradiation could be a good substitute for neutron irradiation, which occurs in operating nuclear installations. However, the ion irradiation does not make a sample radioactive, enabling the mechanical testing of such a sample. Although, only a thin layer of material is damaged. The

conducted Stopping and Range of Ions in Matter (SRIM) software simulations, shown in Figure 18, reveal that the peak damage is located at a depth of 1.80 µm from the surface. The nanoindentation results, which are also shown in Figure 18, illustrate the hardening of both samples after irradiation. The increase in hardness is a common effect after irradiation due to the creation of irradiation-induced defects. Therefore, smaller hardening indicates better ion-irradiation resistance. In the case of the studied FeCrAl-ODS samples, the hardening is relatively small. The M8 sample (vanadium-containing sample) shows hardening slightly lower than the M4 sample (vanadium-free sample). Moreover, it should be noted that the M4 sample was irradiated only up to 1 dpa, while the M8 sample was irradiated up to 5 dpa. Therefore, the nanoindentation results show better irradiation resistance of the M8 sample.

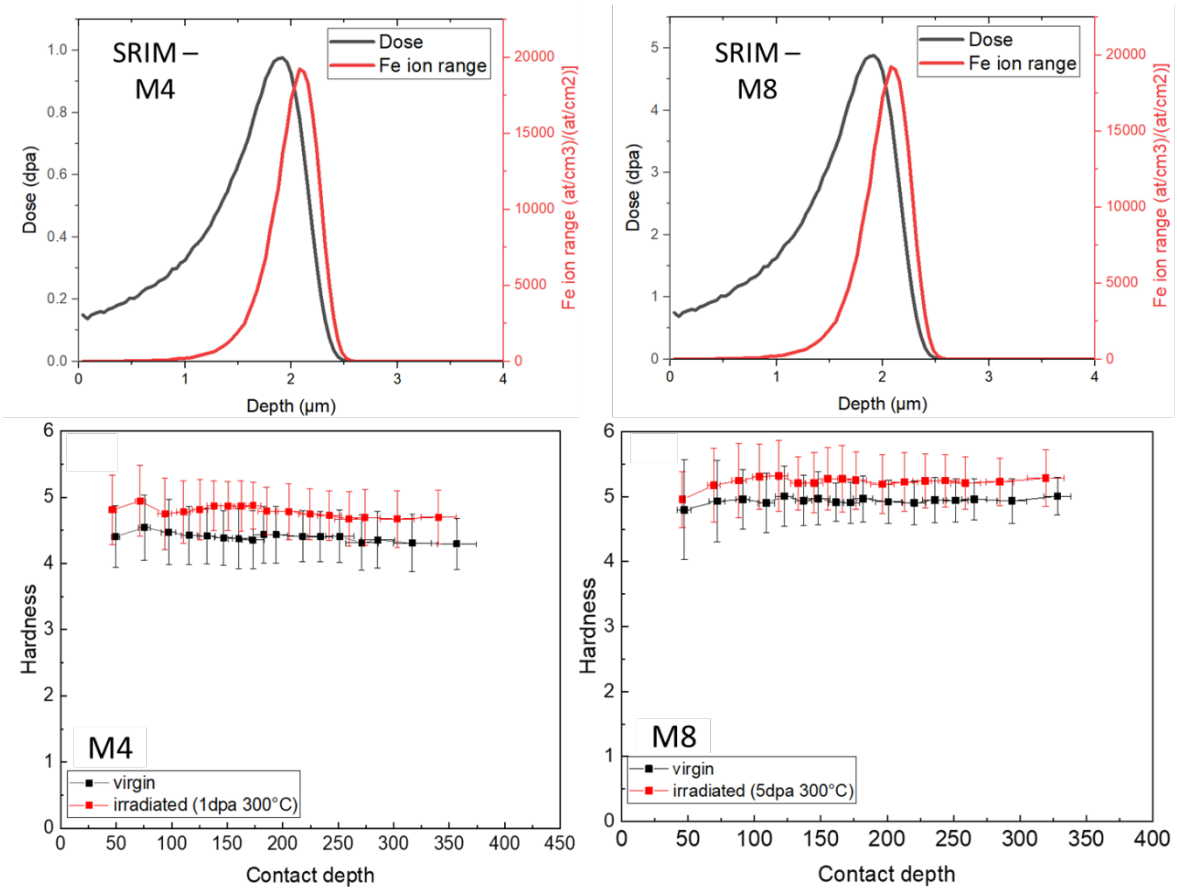

Figure 18: Results of ion irradiation profiles calculated using Stopping and Range of Ions in Matter (SRIM) software and nanoindentation results of virgin and ion irradiated FeCrAl-ODS M4 and M8 samples.

This is attributed to the addition of vanadium, which results in a higher volume fraction of nanometric precipitates. Nanometric precipitates can act as sinks for irradiation-induced defects, therefore mitigating the ion irradiation damage to the material. The grazing incident XRD results show some changes in the structural parameters of FeCrAl-ODS alloys. These results are summarized in Table 4. The lattice parameter of the matrix bcc phase is similar before and after ion irradiation. The crystallite size increases after irradiation in both samples; however, the increase is more pronounced in the M8 sample, which was subjected to irradiation up to 5 dpa vs. 1 dpa for the M4 sample. The microstrain parameter increases after irradiation in both samples, and the increase is more significant in the M8 sample.

Table 4: Results of grazing incident beam XRD of virgin and ion irradiated M4 and M8 samples, where a_{bcc} is the lattice parameter of matrix bcc phase, d is the volume-weighted average crystallite, and ε_0 is a microstrain parameter.

Sample	a_{bcc} [Å]	d [nm]	ε_0
M4 (virgin)	2.8850	218	0.00018
M4 (irradiated 1 dpa)	2.8846	420	0.00030
M8 (virgin)	2.8853	198	0.00020
M8 (irradiated 5 dpa)	2.8850	>1000	0.00089

3.4 Outcomes and development prospects

The eight compositions of FeCrAl-based ODS alloys with Y_2O_3 oxide and V, Ti additions were selected as promising materials to have excellent mechanical properties at elevated temperatures close to the operating temperatures of generation IV reactors including GFRs and high temperature gas-cooled reactors (HTGRs). The investigation done within WP2: Advanced manufacturing processes and materials, showed the successful preparation of FeCrAl–ODS alloys with Ti and V additions by powder metallurgy (mechanical alloying and spark plasma sintering) and controlled heat treatment. The mechanically alloyed powders consist of two bcc solid solutions with similar lattice parameters, confirming the correctly selected mechanical alloying parameters. Powder analysis results showed a significant decrease in crystallite size from 74 nm (pure Fe powder) to about 25 nm during mechanical alloying. The obtained powders were homogeneous, as confirmed by the SEM–EDS micro areas chemical analysis.

The consolidated samples and the annealed samples showed good densification (density of about 96%) and a fine microstructure of α-ferrite with the majority of grains below 1 μm. In addition, the analysis revealed a bimodal distribution of α-ferrite grains after SPS consolidation. In turn, the heat treatment did not significantly affect the bimodal microstructure and grain size. The microstructural analysis showed the presence of nanometric precipitates and their homogeneous distribution in the matrix, which should substantially impact the creep strength and radiation resistance during operation in nuclear conditions. In both groups of materials (after SPS and after subsequent annealing), many nano (20–50 nm)- and micro (up to 1 μm)-oxide and -carbide precipitates are formed, both in the matrix grains and at the grain boundaries.

TEM and STEM-EDS investigations of FeCrAl-ODS alloys enabled the determination of the volume fraction of nanometric precipitates (< 100 nm). The results show that the samples with the addition of vanadium contain a higher volume fraction of precipitates due to the ability of vanadium to form carbides and oxides. The chemical composition analysis showed different types of complex nanometric oxides, most enriched in aluminium. Nanometric oxides are also enriched in yttrium and aluminium (Y-Al-O) or titanium and yttrium (Y-Ti-O). Moreover, precipitates enriched in titanium and carbon were detected, highlighting the formation of nanometric carbides. Nanometric vanadium-rich oxides and carbides were found in the samples with the vanadium. After homogenization annealing at 1020°C, the characterisation of FeCrAl-ODS samples reveals a slight increase in density and relatively stable microstructure with minimal grain growth.

Tensile tests performed with miniaturised samples revealed yield strength between 800 MPa and 950 MPa, and hardness tests show that the addition of V has a positive effect on the increase in the hardness after annealing (on an average by about 24 HV0.5). Moreover, the aging heat treatment at 475°C for 1000h was performed to evaluate embrittlement due to matrix phase separation to Cr-rich and Fe-rich phases and there was no growth of precipitates during annealing. The results showed also very limited embrittlement of the investigated FeCrAl-ODS alloys. Additionally, the ion irradiation at 300°C up to 5 dpa performed at HZDR facilities in Germany enabled the investigation of their radiation damage resistance. The ion irradiation experiments reveal relatively small irradiation-induced embrittlement,

which is attributed to the nanometric precipitates, that can act as sinks for irradiation defects, improving irradiation resistance. However, more investigations on TEM are necessary to confirm such effects.

The obtained results show the promising behaviour of these materials for application in selected parts of Generation IV reactors, including GFRs. However, further investigations on FeCrAl-ODS alloys will be continued at NCBJ, and will focus mainly on mechanical testing (tensile tests) at high temperatures (between 500 and 1000 °C). Moreover, fractographic analyses will be performed to determine the characteristics of the fracture of the FeCrAl-ODS alloys after RT and HT tensile tests. In addition, thermal analyses will be also performed to better understand the structure behaviour of FeCrAl-ODS alloys at high-temperature conditions.

4 PROCESSING OF INCONEL ALLOY 617

4.1 Material and processing requirements

The requirements for SafeG, particularly the ALLEGRO demonstrator, were evaluated to inform the development of a strategy for processing the selected material. From this perspective, the higher temperature requirements of approximately 850 °C, and related design considerations documented in associated deliverables, were crucial when selecting Inconel alloy 617 (IN617). Other material requirements and processing considerations were investigated to establish a basis for initiating empirical investigations, with the geometric features of critical ALLEGRO components, and process input variables identified from existing literature informing the DoE.

Key processing characteristics of alloy 617, include good formability and ease of fabrication, which allows for manufacturing of components and complex structures, using conventional techniques such as pressing, bending, and drawing, without cracking or excessive work hardening. It is also weldable, which is a crucial characteristic for joining and fabrication using techniques such as gas tungsten arc welding (GTAW) and gas metal arc welding (GMAW). However, it is susceptible to hot cracking during welding operations, due to a combination of factors, including its microstructure and high temperatures characteristics. Specifically, alloy 617 loses its ductility at higher temperatures (1175°C to 1330°C). Within this range, also known as the high-temperature brittleness range (HTBR), the material becomes more brittle, and thus prone to cracking when under stress. Correspondingly, the grain boundaries can be affected by the heat applied during the welding process, whereby partial melting can cause discontinuities in material, making it possible for cracks for form in this state [33]. Furthermore, as the material begins to cool, some of the liquid or partially melted material, which is brittle, and thus weaker, may be retained during solidification, with the limited flow of liquid metal and the stress introduced by the crystallisation process itself contributing to the formation and propagation of cracks [34]. The machining of Inconel 617 is also challenging [35,36], due to its high strength and tendency to work harden [37–39], with processing parameters and associated variables [40,41], such as metal chips, dust, and coolant residue, contributing to precision and quality issues. Consequently, special tools and techniques are required to achieve an optimal outcome.

In general, alloy 617 offers a good balance between formability, weldability, and machinability, but higher performance requirements, particularly for GFRs, necessitate the investigation of more specialised techniques to achieve the desired outcomes, both in terms of the material and geometric characteristics. However, there are manufacturing challenges stemming from these requirements, including the ability to create compliant alloy 617 materials and components that can fulfil the demanding duties for these GFR applications [42], as well as the suitability of the different advanced manufacturing technologies under consideration.

The general roadmap used for the manufacturing, processing, and testing of the Inconel alloy 617 is presented in Figure 19.

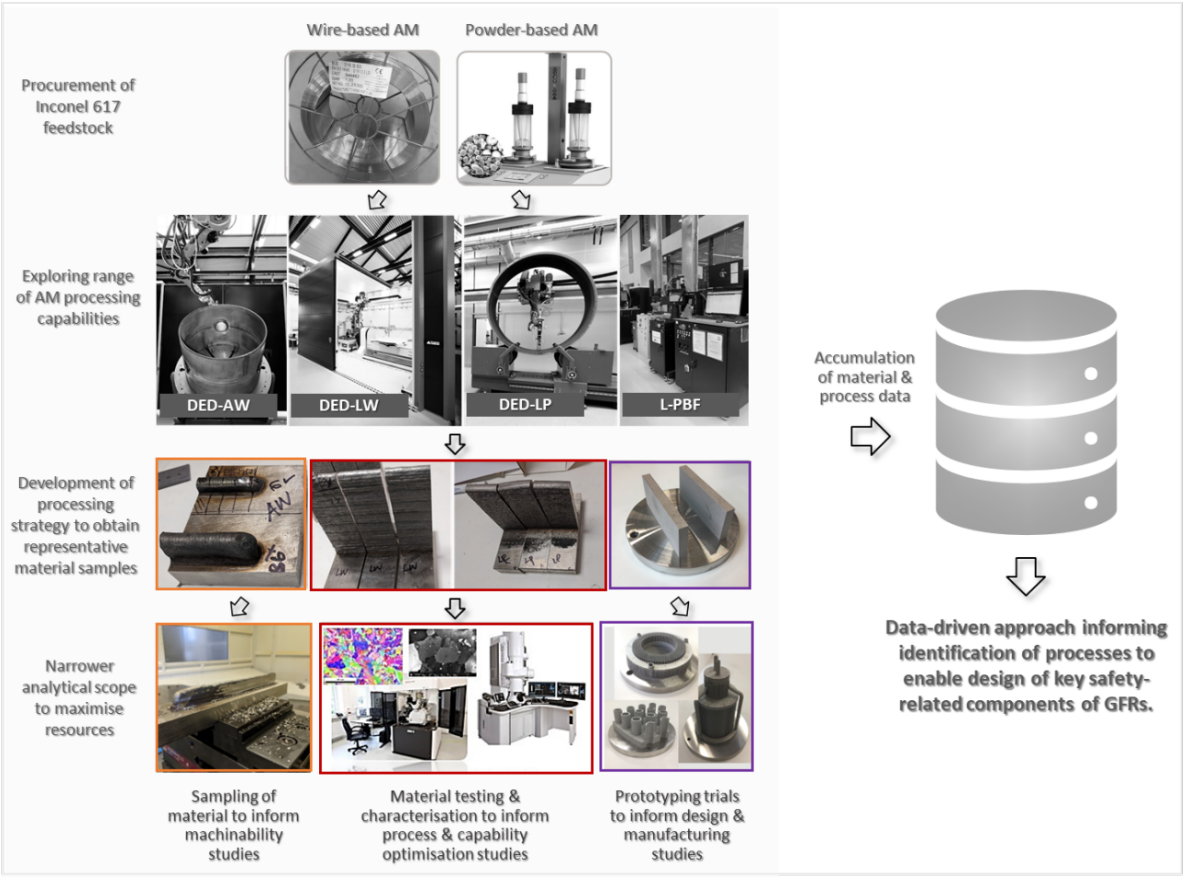

Figure 19: Inconel alloy 617 material processing and testing roadmap.

The initial processing scope was relatively broad, including two of the most prominent classes of AM technologies, namely directed energy deposition (DED) and powder bed fusion (PBF), and both powder and wire feedstock materials, which are typically associated with these technologies. The analytical scope was much narrower and specifically tailored to maximise project resources. This was achieved by designating materials for specific purposes, including the utilisation of the materials derived from the DED arc-wire (DED-AW) capability for developing the machining strategy. Correspondingly, laser powder bed fusion (L-PBF) was primarily used for prototyping purposes, in order to support broader design and manufacturability studies. Although all materials were similarly processed to obtain representative samples (mainly in the as-deposited and heat-treated conditions), the number of samples obtained from the DED-AW and L-PBF processes were insufficient for comprehensive analytical studies. However, DED laser-powder (DED-LP) and laser-wire (DED-LW) processed materials were adequate for preliminary investigations. The goal was to generate sufficient material, process, and capability data to quantify the specific benefits and associated limitations of the SafeG development strategy. Correspondingly, the materials samples and data generated during this project will support planned investigations that were beyond the initial focus and scope of this study, which explores the feasibility of processing of alloy 617 via additive manufacturing.

4.2 Fabrication and testing

The material development strategy was incremental, including a parametric study, designed to evaluate key process variables, followed by the fabrication and subsequent heat treatment and machining of representative AM samples. While the incremental approach was necessary for facilitating a more comprehensive analysis of the selected technologies, the material processing requirements and related GFR considerations informed the DoE, with outputs and observations from each iteration guiding decisions about the next. The general development approach for the additive manufacturing of alloy 617 is depicted in Figure 20.

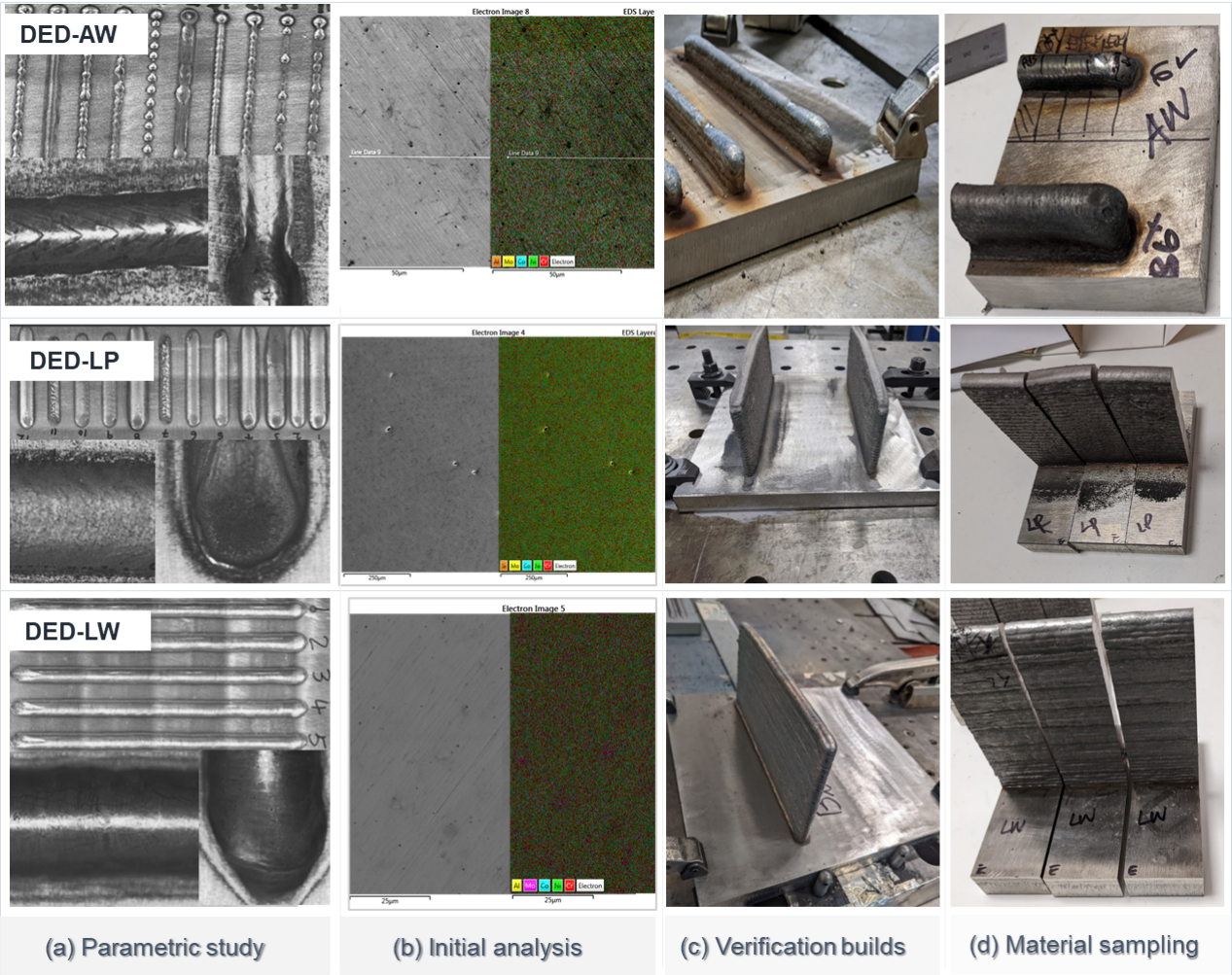

Figure 20: Key DED development stages including (a) deposition and (b) metallographic inspection of linear builds (c) trial build and evaluation of parameters and (d) fabrication of material samples for testing .

The main stages considered include the manufacturability phase, involving the development of parameters to demonstrate that selected AM technologies could fulfil the specific processing requirements for IN617. The next phase was focused on assessing the stability and repeatability of the process to support related activities. While the equivalence and qualification stages are developmentally important for assessing the readiness of these technologies, and by extension, the applications to which they have been applied, for meeting GFR design requirements, these aspects were beyond the scope of the SafeG project but were included in the plan to ensure that broader considerations remained in focus. Ultimately, safety is of utmost importance for the SafeG, particularly the GFR demonstrator ALLEGRO, thus the material development strategy, including related test campaigns, were designed to enhanced understanding of common and specific challenges and their potential implications, within the scope and budget of this project.

4.2.1 Processing capability

Additive manufacturing (AM) technologies and hot-isostatic pressing (HIP) are some of the advanced processing techniques that were initially considered. AM is an innovative and promising technique that combines the formability and weldability of alloy 617, to create more streamlined manufacturing processes that can potentially transform GFR design requirements. Accordingly, the preliminary goal was to determine the suitability of different AM processes, which were investigated alongside innovative subtractive manufacturing or machining techniques to fabricate materials and assess their suitability for and on critical GFR components. Due to the combination of the novel manufacturing

approach and the application criticality, it was essential to establish a strong foundation of evidence to support the adoption of AM technologies for GFR constructions, while reliably informing future developments for the ALLEGRO demonstrator.

Focusing on the core task requirements, and the processing requirements for alloy 617, different AM capabilities were selected from two of the most prominent AM technology classes for processing metals, namely directed energy deposition (DED) and powder bed fusion (PBF), to enhance understanding of the interactions between and within these manufacturing technologies. This approach allowed for the broader analysis of selected AM capabilities, relative to the specific task requirements, while providing insights into the efficacy of each process based on the empirical outputs. The AM capabilities used for the processing of alloy 617 are shown in Figure 21.

(a) (b) (c) (d)

Figure 21: Capabilities used for processing of alloy 617 including (a) Arc-wire DED (b) Laser-powder DED (c) Laser-wire DED and (d) Laser powder bed fusion (LPBF).

Open architecture (OA) systems are typical for DED technologies, and different configurations were used for experiments. The arc-wire or AW-DED configuration is a multi-axis robotic system with interchangeable gas tungsten arc welding (GTAW) end-of-arm tooling (EOAT) for wire deposition. Two laser DED systems were utilised; a laser powder (DED-LP), comprised of a 15kW Laserline fibre-coupled diode laser, gantry-mounted multi-axis robot arm, and a coaxial end-effector for powder deposition, and laser wire (DED-LW) capability, with a 16kW Trumpf fibre-coupled disk laser, gantry-mounted robot arm, and wire-feeding system. Two L-PBF systems were utilised, the Aconity Mini platform for rapid material prototyping, and the Aconity Lab, for larger builds. The Aconity systems use a continuous-wave 1064nm Nd:YAG laser for processing powder feedstock.

4.2.2 Material Development

Key processing considerations, including formability, temperature, and other related experimental variables, identified from literature, were used to inform the DoE for initial trials. The experimental aim was to identify a suitable processing range for depositing the required material samples before selecting the variables provided in Table 5.

Table 5: Initial experimental matrix for depositing alloy 617.

Category	Experimental Variables	DED-AW	DED-LP	DED-LW
Equipment	Energy source	Arc	Laser LDF 15000	Laser TruDisk 16002
	End-of-arm tooling (EOAT)	TOPTIG	Fraunhofer COAX8	Precitec YW52
	Fibre core diameter (µm)	-	1500	400
	Collimating lens (mm)	-	72	200
	Focusing lens (mm)	-	500	300
	Spot Size (mm)	-	9.91	60
	Carrier gas (Argon) (l/min)	-	10	-
	Purge gas (Argon) (l/min)	17	30	150
Input parameters	Power (kW)	2	8	10
	Material feed rate	1.5 m/min	83 g/min	8 m/min
	Travel speed (mm/min)	102	500	800
	Feedstock	Ø1.2mm wire	50-150 µm powder	Ø1.2mm wire
	Layer offset distance (mm)	~1	~2	~1.6

Initial screening experiments consisted of depositing single beads of the IN617 powder and wire feedstock onto 20mm thick stainless steel 316L substrates, before completing visual and microscopic inspections. The insights from these outputs were used for further refinement of the build strategy, including the selection of processing parameters (Table 5) eventually used for verifications builds. The resulting builds were subsequently separated from the substrates, to obtain individual material samples for post-DED investigations, as depicted in Figure 20(c). Next, representative sections were obtained from all DED builds (Figure 20(d)), to allow for the isolation and analysis of the relative material characteristics, attributable to specific DED techniques, builds, and/ or post-DED procedures. Correspondingly, the intermediate focus was on evaluating the effects of different heat treatment (HT) protocols on resulting IN617 materials.

The L-PBF procedure involved the rapid sequential production and metallographic preparation of multiple metal coupons, which were designed to fit directly into an existing Struers' polishing systems. Eight coupons were produced in total, each containing 17 x 32mm cubes, with each cube printed with a different laser parameter set. This approach accelerated the development phase, as only a single build with different parameters sets was required, to provide insights into the processing window of the alloy, further reducing material development costs. The key stages of the L-PBF material development process are depicted in Figure 22.

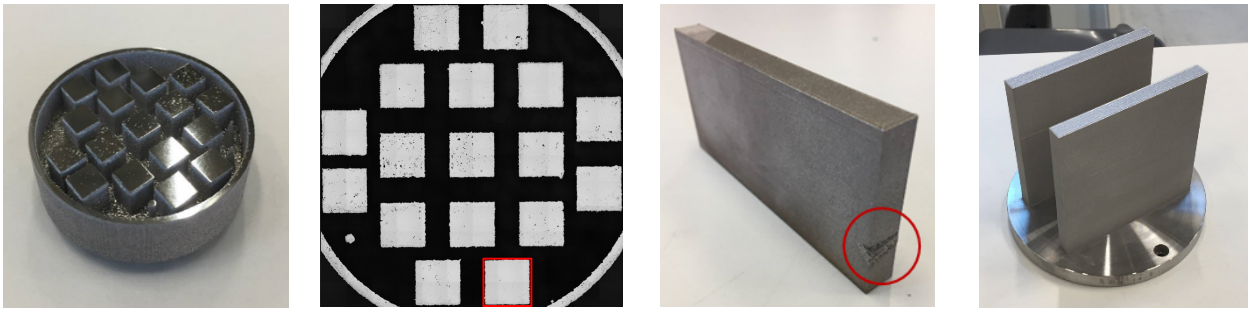

(a) (b) (c) (d)

Figure 22: Key LPBF development stages including (a) deposition and (b) metallographic inspection of coupons (c) trial build and evaluation of parameters and (d) fabrication of materials for characterisation and testing.

A typical example of one of the 17-cube polishing samples is shown in Figure 22(a). Porosity is visible even to the naked eye in some sections, making this a very useful tool for rapid screening of parameters. The manufactured coupons were removed from the substrate with a soft tap hammer, before polishing and imaging the target surfaces, to provide insights into the processing window. Polishing was

performed using a Struers Tegramin-20 and parts were imaged using an Olympus optical microscope with a Clemex imaging system. Analysing the density of coupons can also augment inspection data, by facilitating the rapid selection of parameters. For instance, the coupon highlighted using a red square, in the mosaic image, derived from the Olympus microscope Clemex software (Figure 22(b)), denotes the most dense sample from this coupon.

Material samples of size 10x100x100mm were produced in an upright orientation, based on the parameters determined from the rapid coupon prototyping methodology. The laser power was set to 160W, with a scanning speed of 1700mm/s, hatch spacing of 45µm, and layer thickness of 30µm. The meander hatch rotation strategy was selected, starting at 45° and rotating by 90° per layer. For this phase, two attempts were required, as the first attempt was unsuccessful, due to inherent and evident processing inefficiencies. The resulting flaw is shown in area encircled in red, in Figure 22(c). This defect was caused by a combination of factors, including insufficient dosing and low powder spreadability or flowability attributed to particle size distribution, while a system error, which resulted in the early termination of the process, further impeded the achievement of the desired build height of 100mm.

However, after sectioning the build, the inspected surfaced were deemed to be of acceptable quality, with minimal porosity occurring within the material. The observations from this trial were used to refine the build strategy before proceeding with a second build. This attempt was successful, with resulting builds progressed for further investigations. Similarly, the main consideration was how to maximise resources, whilst obtaining sufficient information to support feasibility assessments.

4.2.3 Heat treatment

A heat treatment procedure is recommended to eliminate relaxation cracking for Inconel alloy 617 components used in extreme environments. From accessible literature an annealing range of 1160°C to 1200°C is recommended, but the focus was on evaluating the effects of different heat treatment strategies, including the possibility of applying a two-step procedure to remove any potential segregation effects, before increasing the temperature, to fully homogenize the material. Equally, the cooling rate significantly affects the final properties of the material, and it was strategically important to establish the effects of heat treatment on the different AM material samples. Specifically, DED builds are typically characterised by considerable anisotropy and heterogeneity, necessitating post-deposition heat treatments to improve material properties and performance. However, there is limited understanding of the condition and effects of additively manufactured alloy 617 materials, especially for the targeted application. For other Nickel based alloys, homogenization treatments are normally applied at lower temperatures, relative to the alloy melting range (1332°C -1380°C). Thus, within the available budget, it was empirically expedient to proceed with a fixed temperature or single step heat treatment procedure to which different cooling rates were applied. The preliminary aim of the procedure was to homogenize the materials, to address any segregation effects derived from the DED process, using the recommended solution annealing temperature of 1175°C, as defined by Special Metals. The samples were split into 3 batches, for water quenched (WQ), air cooling (AC) and furnace cooling (FC), before assessing the resultant properties.

4.2.4 Machining

The machining strategy was developed using alloy 617 material samples derived from the arc-wire DED process, with insights gained from the literature surveys facilitating the selection of the tools and cutting conditions defined for initial machining trials. These preliminary tests used high pressure soluble coolant (HPSC) and supercritical CO_2 ($scCO_2$) with Minimum Quantity Lubrication (MQL) cooling strategies. The purpose was to assess and compare the capability of selected cutting tools for machining the sacrificial materials, using both HPSC and $scCO_2$+ MQL. The overall approach and key capabilities used for machining are presented in Figure 23.

(a) (b) (c)

Figure 23: Development of finishing strategy facilitated by (a) Starrag HEC 1800 machine tool and (b) Pure-Cut Plus Fusion coolant system, and (c) intermediate output for analysis.

The machining of the representative AM samples (Figure 20) were conducted on the Starrag HEC 1800 machine tool (Figure 23(a)), supported by the Fusion Pure-Cut Plus coolant system (Figure 23(b)) that controls and deploys a constant stream of $scCO_2$ mixed with MQL oil to the cutting tool on the machine. The soluble oil coolant used on the Hec1800 is Hocut 795N. High pressure CO_2 is heated up to 40°C for the CO_2 to reach a supercritical state. The system then uses an oil dosing pump to inject MQL lubricant into the $scCO_2$ stream. A mixture of $scCO_2$+MQL flows to the tool holder and cutting edge. The $scCO_2$+MQL unit can be triggered manually through a built-in display or via M-codes in the CNC program.

The trials consisted of machining one side of the test samples with HPSC and the other side with $scCO_2$+MQL to compare the cutting forces, surface roughness and tool wear. The setup for the machining process involved clamping the samples in a small vice that is placed on top of an adaptor plate on the dynamometer to capture forces during the machining process (Figure 23(c)). The dynamometer used was a Kistler 9255C, 260 x 260 mm sized with an adaptor plate on top to securely attach the small vice that holds onto the samples. Due to the rough and uneven nature of the ad-deposited DED samples (Figure 20), a roughing pass was necessary to obtain flatter surfaces, relative to the machine tool, and to facilitate subsequent finishing passes with the chosen tools.

The roughing step was carried out with an on-machine tool; this data was not required as it is only carried out to facilitate the finishing passes to be conducted. The finishing tools to be tested were the Mitsubishi ARP5PR2503SA25M and the Sandvik 419-036C3-14L. These tools were chosen due to their previously known compatibility with $scCO_2$+MQL systems, as they are both capable of through tool coolant, and both can be modified to have cooling nozzles installed using knowledge gained through the literature review. The respective tool manufacturers were contacted to identify the insert grades that would be most suitable for machining Inconel 617. Sandvik recommended the 419R-1405M-PM 1130 insert, along with recommend cutting conditions; previous project work with this tool achieved average roughness (Ra) values of 1 to 1.5 µm. Mitsubishi recommended the RPHT1040M0E4-M MP9130 (RPHT) and RPMT1040M0E4-M MP9130 (RPMT) inserts. The first was suggested due to its “excellent positional accuracy and finish” while the second was recommended due to its rounder edge hone providing “more strength and heat resistance” to the insert. The HPSC tests were carried out at 50 bar of through tool pressure (using Hocut 795N oil) while the $scCO_2$+MQL tests had a flow rate of around 40 kg/hr, with an MQL flow rate of 2 ml/min (NuCut Plus oil).

The initial tool tests on the DED-AW materials (Figure 20), which were used for these trials. The materials were machined with HPSC on one side and with $scCO_2$+MQL on the other, hence 6 tests were carried out.

The cutting conditions used for these tests using each tool and insert combination is shown in Table 6.

Table 6: Initial tool testing cutting parameters.

Tool Used	Insert Used	Cutting Speed (m/min)	Spindle Speed (RPM)	Table feed (mm/min)	MRR (cm^3/min)	DoC (mm)	Feed Per Tooth (mm)	Width of Cut (mm)
Mitsubishi ARP5PR2503SA25M	RP**H**T1040M0E4-M MP9130	35	446	201	3.4	1.0	0.15	16.8
Mitsubishi ARP5PR2503SA25M	RP**M**T1040M0E4-M MP9130	35	446	201	3.4	1.0	0.15	16.8
Sandvik 419-036C3-14L	419R-1405M-PM 1130	40	354	566	12.3	1.0	0.80	21.75

Regarding the cutting forces and tool life between the three tool and insert combinations, there were no discernible differences. This is due to the low cutting conditions and the short cutting distance, thus not providing enough work for the insert to begin showing significant amounts of wear and highlighting the different rates of wear between them. However, there were clear differences in terms of surface roughness between the three combinations of tools and inserts. Surface roughness was measured using a Mitutoyo Surftest SJ-410, in accordance with ISO1997. Analysing the surface roughness values of the samples by only comparing HPSC and $scCO_2$+MQL, it is evident that in every case $scCO_2$+MQL can achieve a lower Ra, Rq and Rz value independent of the tooling or insert.

Table 7: Evaluation of selected cutting tools based on machining trials and ouputs.

		Roughness			Average	Average	Average	STDVE	STDVE	STDVE
AW1 HPSC		1	2	3	Ra	Rq	Rz	Ra	Rq	Rz
	Ra	0.657	0.652	0.653	0.654			0.003		
	Rq	0.769	0.764	0.764		0.766			0.003	
	Rz	3.118	3.05	3.054			3.074			0.038

		Roughness			Average	Average	Average	STDVE	STDVE	STDVE
AW1 scCO2+MQL		1	2	3	Ra	Rq	Rz	Ra	Rq	Rz
	Ra	0.619	0.617	0.618	0.618			0.001		
	Rq	0.705	0.703	0.704		0.704			0.001	
	Rz	2.524	2.528	2.515			2.522			0.007

		Roughness			Average	Average	Average	STDVE	STDVE	STDVE
AW2 HPSC		1	2	3	Ra	Rq	Rz	Ra	Rq	Rz
	Ra	0.449	0.448	0.448	0.448			0.001		
	Rq	0.544	0.544	0.544		0.544			0.000	
	Rz	2.455	2.458	2.463			2.459			0.004

		Roughness			Average	Average	Average	STDVE	STDVE	STDVE
AW2 scCO2+MQL		1	2	3	Ra	Rq	Rz	Ra	Rq	Rz
	Ra	0.232	0.233	0.229	0.231			0.002		
	Rq	0.282	0.283	0.279		0.281			0.002	
	Rz	1.21	1.254	1.165			1.210			0.045

		Roughness			Average	Average	Average	STDVE	STDVE	STDVE
AW3 HPSC		1	2	3	Ra	Rq	Rz	Ra	Rq	Rz
	Ra	0.753	0.75	0.751	0.751			0.002		
	Rq	0.979	0.978	0.978		0.978			0.001	
	Rz	4.483	4.509	4.545			4.512			0.031

		Roughness			Average	Average	Average	STDVE	STDVE	STDVE
AW3 scCO2+MQL		1	2	3	Ra	Rq	Rz	Ra	Rq	Rz
	Ra	0.656	0.656	0.656	0.656			0.000		
	Rq	0.794	0.795	0.794		0.794			0.001	
	Rz	3.198	3.193	3.183			3.191			0.008

AW1 = Mitsubishi RPHT inserts, AW2 = Mitsubishi RPMT inserts and AW3 = Sandvik tool.

When comparing the Mitsubishi tool to the Sandvik high feed tool (AW1 & AW2 vs AW3), a better surface finish was achieved with the Mitsubishi tools in every metric measured (AW1 and AW2). Furthermore, when comparing the two Mitsubishi inserts, represented by AW1 and AW2 (RPHT and RPMT respectively), every metric indicates that the AW2 RPMT inserts produce superior surfaces, in terms of the Ra, Rq and Rz values. Therefore, the RPMT insert with the Mitsubishi tool was used for the rest of the trials, as this provides the best surface results.

A total of eight samples were machined using the Mitsubishi tool and RPMT1040M0E4-M insert. The same cutting conditions were used as before (Table 7), but with an adjusted depth of cut (DoC) of 0.1mm to achieve a better surface finish and reduce the material being removed. The thicknesses of the samples post machining varied due to the differences in build parameters and the amount of material required to be taken off to be able to conduct the finishing passes. It is important to note that the thinner the samples are the more prone they are to vibrating and deflecting from the cutting tool, thus potentially showing inferior surface finishes. The samples fin height varied, it ranged from 71 to 96 mm. Due to the clearance required between the tool holder and the bottom section of the samples to avoid collision. Only four runs on finishing passes were able to be conducted. These runs were calculated using the shortest sample in order to have the same number of runs between all 8 samples. Each sample was machined using HPSC on one side and $scCO_2$+MQL on the other side, before comparing the machined surfaces. The resultant cutting forces and effects of selected parameters on tool wear were also evaluated. The machining setup and resulting surfaces are shown in Figure 24.

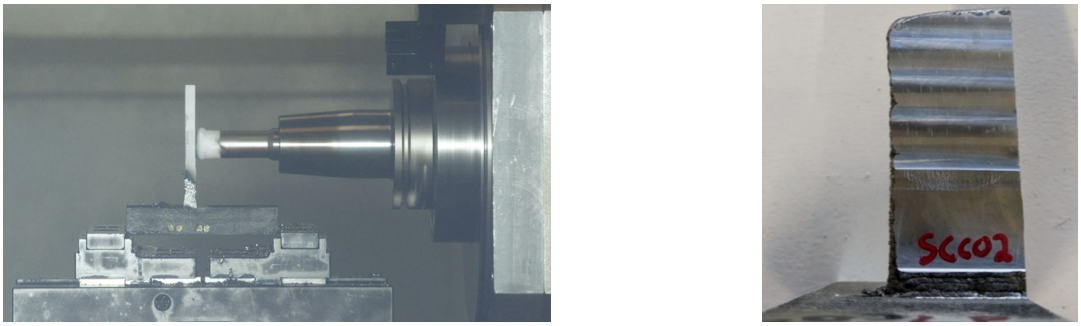

(a) (b)

Figure 24: Implementation of machining strategy for laser-powder and wire DED samples including (a) tool holder and sample arrangement and (b) typical output.

In terms of tool wear comparison, there was not sufficient machined material to wear out the tools enough to be able to distinguish large differences between each sample as only 4 light finishing passes were conducted with each fresh insert. However, there were some observable differences, which are documented in the following paragraphs.

There was no discernible difference observed in relation to samples 1 to 5, as the tool inserts appear to have very similar amounts of wear when using HPSC and $scCO_2$+MQL, as seen along the lower edge of the images presented in Figure 25(a). However, when comparing inserts used for the HPSC and $scCO_2$+MQL surfaces of the LW-AC sample (Figure 25 (b)), there are visible chips on the inserts, even at such low wear rates. Similarly, chips were observed along the edge of inserts used for the LW-FC and the LW-WQ samples, as shown in Figure 25 (c) and (Figure 25 (d) respectively.

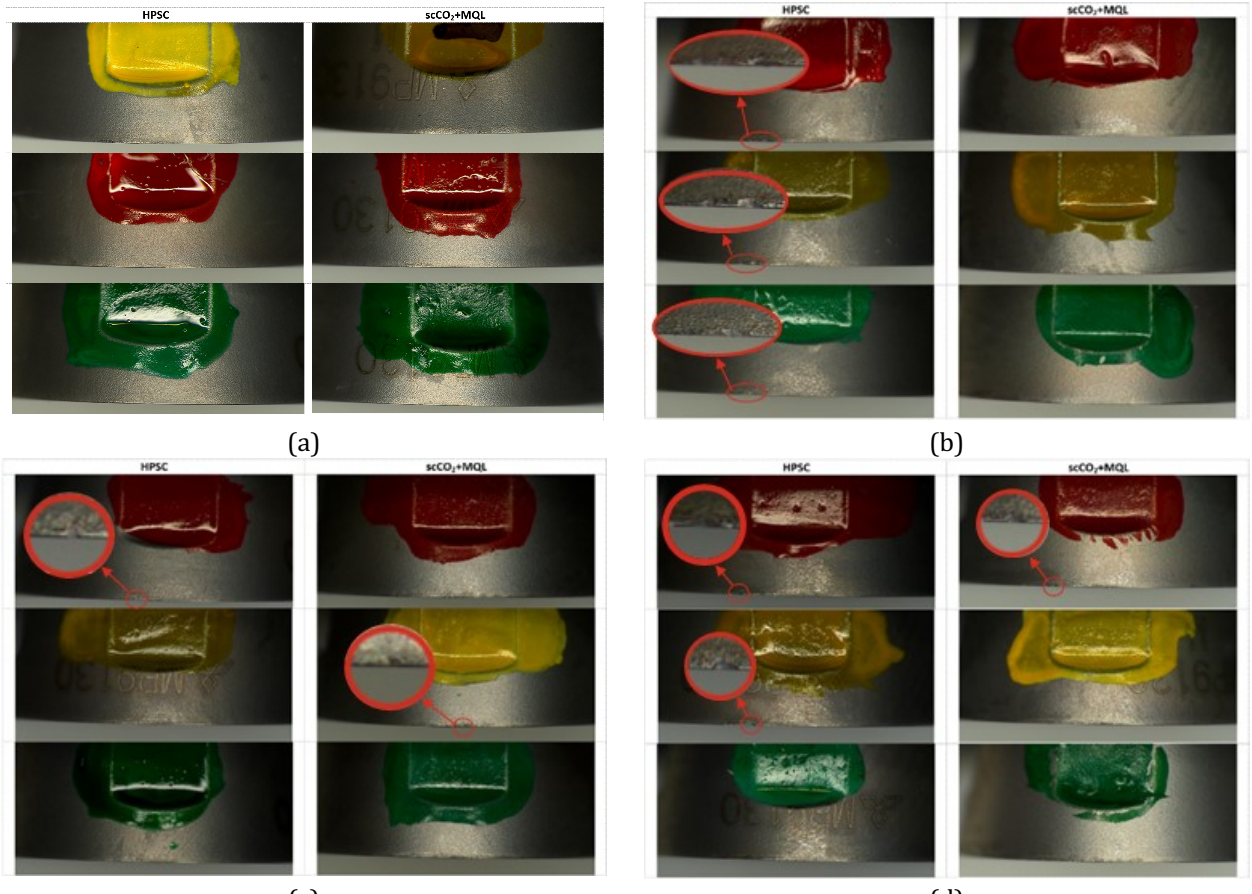

(a) (b)

(c) (d)

Figure 25: Analysis of (a) tool wear comparison between HPSC and $scCO_2$+MQL for samples 1 to 5 and tool wear comparison between different cooling methods for (b) LW-AC (c) LW-FC and (d) LW-WQ sample.

Increased tool wear was expected when machining the heat-treated samples as the hardness of the material had increased compared to the as built samples. However, it is noteworthy that tool wear was indiscernible on all laser powdered heat-treated samples while all the laser wire heat treated samples caused the inserts to chip at least once. Based on these limited trials, it appeared that the DED-LP materials were relatively more machinable than the DED-LW materials.

The force data from each sample were as expected when monitoring the cutting process in real time, hence two scenarios were used to provide further insights. Scenario 1 is comparing the largest delta between the same sample machined with HPSC and $scCO_2$+MQL, LP-AC, and the second scenario is comparing the lowest and highest achieved roughness values independent of cooling strategy, for LP-WQ and LW-AC samples. Scenario (1) highlighted in yellow, and scenario (2) highlighted in red, as shown in Figure 26.

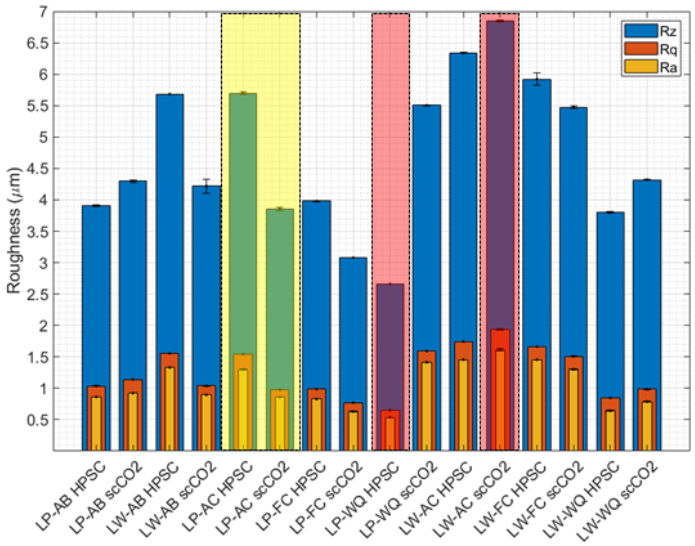

Figure 26: Comparision between force data, surface roughness and machining conditions.

When comparing the forces for the LP-AC samples (Figure 26), based on the Ra values from both types of material, it appears that a higher cutting force contributed to better surface finish. The higher forces were attributed to the extra cooling effect of the $scCO_2$ on the material, relative to the typical heat build-up associated with the use of HPSC. However, there were observable differences when comparing the force data, based on the lowest (0.5 µm) and highest (1.6 µm) Ra values, measured for LP-WQ HPSC and LW-AC $scCO_2$+MQL samples, respectively. There were variations in the magnitude and direction of the output data, which represents the four distinct cuts taken from each of the samples Furthermore, when comparing the force data and roughness values (Figure 26), there appeared to correlations between the cutting force and resulting surface finish, whereby higher cutting forces typically resulting in a better surface finish. However, due to the low sampling rate, further investigation is necessary to enhance understanding of the complex interactions between machining parameters, process variable, and the observable effects. The cutting force data, acquired during the machining process, is shown in Figure 27.

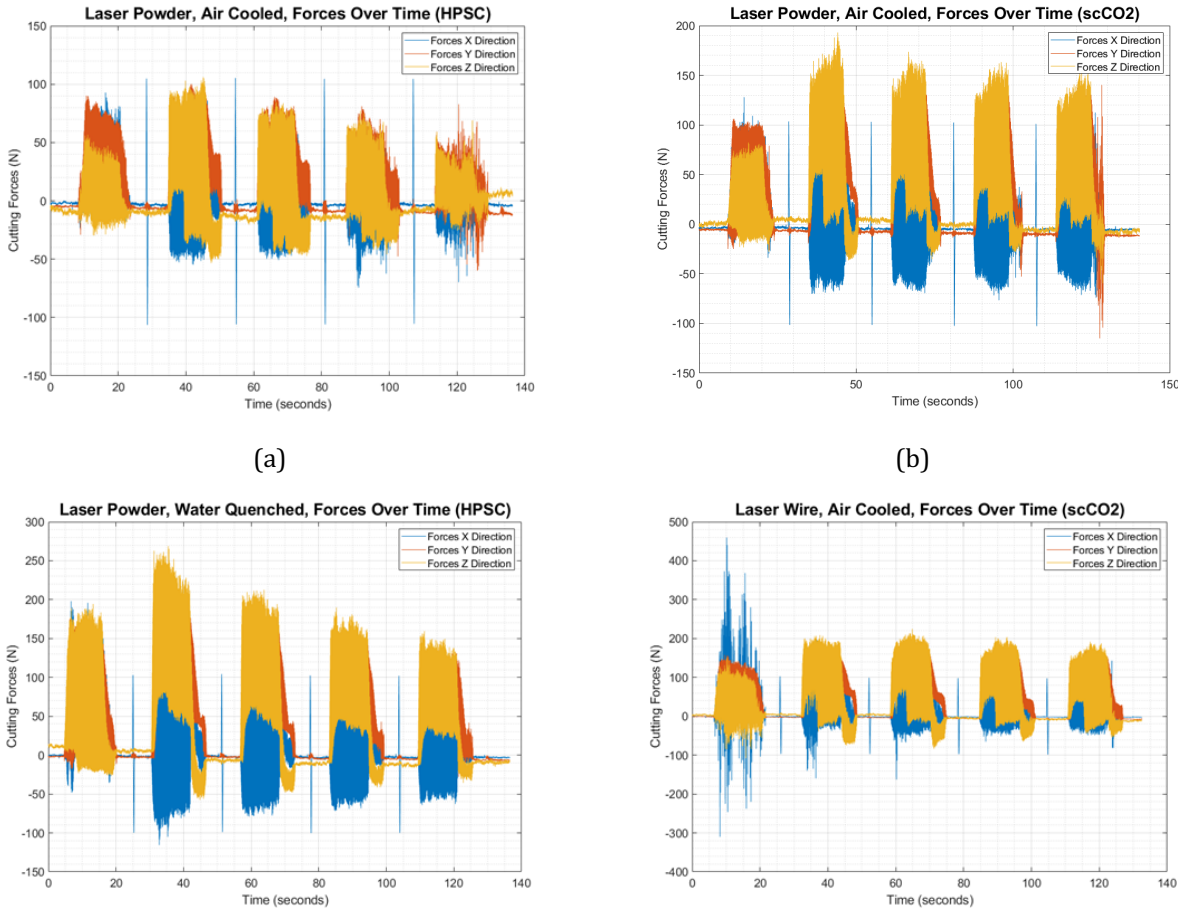

Figure 27: Analysis of selected scenarios (a) LP-AC forces of HPSC run and (b) $scCO_2$+MQL run for Ra=1.3 µm and Ra=0.9 µm respectively, and (c) LP-WQ forces of HPSC run and (d) LW-AC $scCO_2$+MQL run for Ra=0.5 µm and Ra=1.6 µm respectively.

4.2.5 SafeG Demonstrator

Manufacturing and related considerations were investigated as part of the overall material development strategy for SafeG. This final empirical stage was primarily initiated to enhance understanding of the benefits and limitations of advanced manufacturing processes for specific applications in the nuclear industry. A case study approach was adopted to ensure that specific insights were realistically informed, and a scaled-down model of the DHR HX part was selected. This SafeG demonstrator part is depicted in Figure 28.

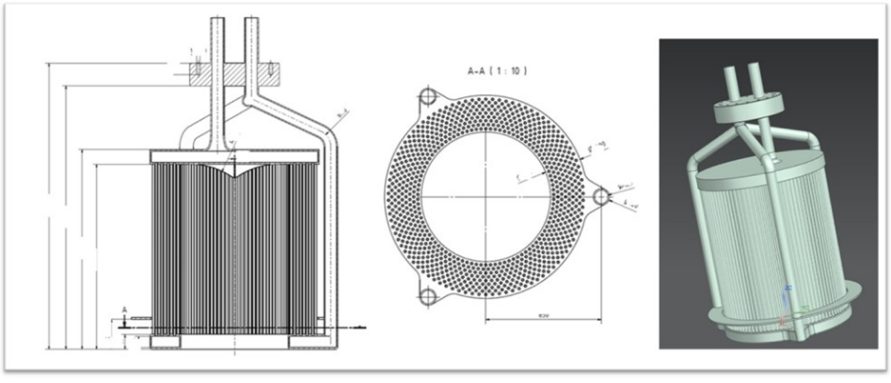

Figure 28: SafeG demonstrator.

The initial attempt to print this part (with supports under the lower ring) was unsuccessful, due to the stresses imparted into the overhanging ring. Such overhanging surfaces are typically affected by overheating and can warp after a couple of layers, which causes the build to fail. Therefore, the build strategy was modified by increasing the thickness of the build supports to counteract this warpage, with a successful demonstrator section produced (Figure 29).

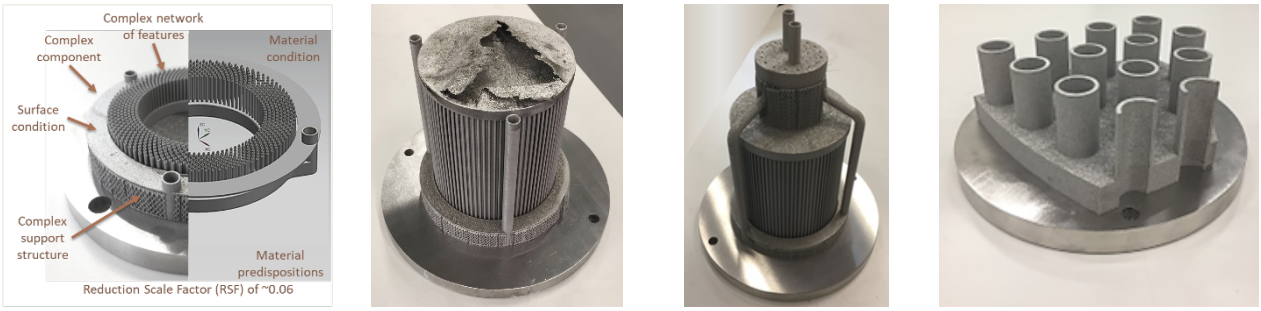

(a) (b) (c) (d)

Figure 29: Key stages in the development of SafeG demonstrator including (a) initial 20mm trial build (b) first and (c) final full build attempts at reduced-scale and (d) section of component built at full/ actual scale.

An initial trial build was completed, for the first 20mm of the component, to ensure evaluate the feasibility of constructing the DHR HX in the current state, without any design modifications. Supports were more densely packed under the overhanging section than previously. A full-height build was then attempted on the Aconity Lab (Figure 21(d)), which is better suited for large builds, as it can be topped up with supplies, without pausing the build or breaking the protective atmosphere. This build progressed well, however a large overhang caused it to fail at 60% of the build height, thus highlighting the need for the proper design of components for AM. For this use case, the strategic introduction of adequate support structures, including modifications to the internal radii and incremental overhangs, can reduce the stresses involved, thereby preventing component warping and failure.

The first attempt at printing the DHR HX component was terminated after ~26 hours, due to the build failing at a large overhang. However, this attempt provided further insights into possible design improvements to be made, including the need to adequately support hollow sections. A second build was attempted, with significant improvements, with a final build completed at a representative scale, thus demonstrating the capability of the process. These outputs also provide a tangible basis for quantifying the issues that must be addressed to achieve the desired end goal of a creating designs that are similar to that used for the actual ALLEGRO demonstrator.

4.3 Results and analysis

A test matrix was developed to facilitate the investigation of the resulting materials. However, due to a combination of factors, including the scope of the campaign, based on the types of tests that were planned and the number of samples to tested, relative to the available resources, it was necessary to prioritise the work. Accordingly, the immediate emphasis was on comparatively assessing DED-LP and DED-LW samples. The microstructure and chemical composition of these samples were assessed by SEM, using a Thermo Fisher Scientific™ Helios™ 5 UX SEM coupled with an EDS detector operating at 20 kV accelerating voltage. The non-machined samples were ground using SiC papers (up to P1000) and electro-polished at 10°C in the mixtures of perchloric acid with methanol at the voltage of 25 V for 50 s.

The observations of the machined surface (from the top view) were performed using a Keyence VHX-7000 digital microscope to investigate the surface topography. The roughness measurements were performed at three different locations on the machined surface of Inconel samples. The roughness

values of Ra, Rq, and Rz were measured. The SEM observations were performed on the cross-section of the machined samples to observe eventual changes in the microstructure near the machined surface. These observations were carried out using a Zeiss EVO MA10 SEM in secondary electron mode. The samples were hot-mounted in conductive material and ground with SiC papers (grade P80 to P2400). The final polishing was performed using diamond suspensions with grain size of 9, 3, and 1 µm. Subsequently, the samples were etched using oxalic acid ($C_2H_2O_4$). EBSD was conducted on the cross-section near the machined surface to evaluate the deformation of the materials. The samples for EBSD were ground with SiC papers (grade P80 to P1000) and then electro-polished at 10°C in the mixtures of perchloric acid with methanol at the voltage of 25 V for 50 s. EBSD analyses were carried out using the EDAX Velocity Pro-EBSD system embedded in Helios™ 5 UX SEM. The maps were acquired using a 20 kV accelerating voltage and approximately 10 nA probe current. The analysis of EBSD data was performed by EDAX OIM Analysis 8 software.

The microhardness tests were carried out on the cross-section of samples prepared for SEM observations. The microhardness measurements were conducted using an HV-1000 Huatec Group microhardness device under a load of 0.4903 N (HV0.05). The series of indents were made at different distances from the machined surface, i.e., at 10 µm, 30 µm, 50 µm, 75 µm, 100 µm, and 200 µm. Five series of measurements were performed for each sample to obtain average values.

The SEM observations of the DED samples show matrix phase and precipitates. Selected backscattered electron (BSE) images and EDS elemental maps are shown in Figure 30. The precipitates appear to be finer in the samples derived from the wire feedstock. Moreover, it appears that annealing followed by water quenching decreases the number and size of precipitates. According to EDS maps (Figure 30(b) and Figure 30(d)), the precipitates are enriched in Cr and Mo. Similarly, the observed precipitates in TEM results can be attributed to M_6C (molybdenum-rich) and $M_{23}C_6$ (chromium-rich) carbides.

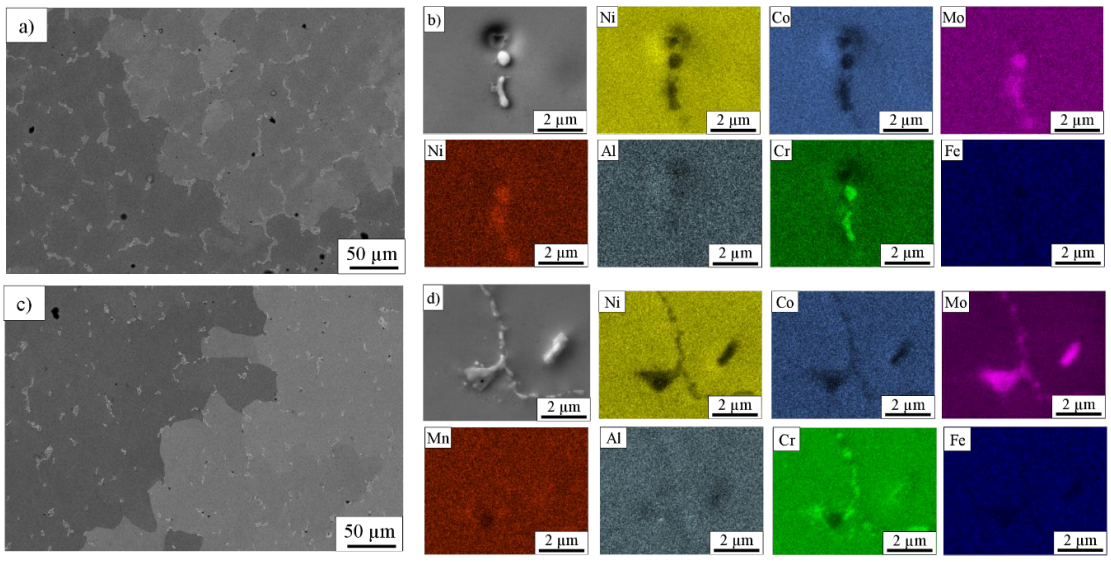

Figure 30: SEM investigations and EDS analyses of additive manufactured samples: a) SEM-BSE image of LP-AD sample, b) EDS elemental maps of LW-AD sample, c) SEM-BSE image of LP-WQ sample, d) EDS-Elemental maps of LW-WQ sample.

The roughness measurements, which are shown in Table 8, reveal some differences between studied samples. The average roughness (Ra) of the samples is between 0.538 µm and 1.415 µm. Therefore, the roughness decreases significantly compared to the samples after additive manufacturing, which show high roughness and poor surface quality. It confirms good results of machining of additively manufactured parts presented by other authors [43,44]. The lowest roughness was found in the LP-WQ-HPSC sample, while the highest roughness was found in the LP-WQ-scCO_2 sample. Therefore, the cooling strategy during machining (HPSC vs scCO_2) seems to impact the roughness significantly. However, for

other samples, the differences in the impact of HPSC and $scCO_2$ are not so important. On the other hand, the sample LW-AD shows a lower roughness after cooling by $scCO_2$ than by HPSC. It is evident that the cooling strategy impacts the surface roughness; however, other factors, such as microstructure, are also crucial in the roughness values after machining of additive manufactured Inconel 617 alloys. The wire or powder feedstock does not seem to impact roughness significantly. The annealing followed by water quenching appears to decrease the roughness (except in the LP-WQ-$scCO_2$ sample). This phenomenon was attributed to the effect of a more homogeneous microstructure after the heat treatment. However, further investigation is necessary to provide further insights.

The results are comparable to the roughness measurement performed in other studies on the machinability of additive manufacture Ni-based superalloys. In the studies concerning additive manufactured Inconel 718, Kaynak et al. [43] found that after machining, the surface roughness is between approximately 0.50 and 1.85 µm, depending on machining conditions.

Table 8: Roughness results (Ra, Rq, Rz) of the machined surface.

Sample	Ra [µm]	Rq [µm]	Rz [µm]
LP-AD-$scCO_2$	0.923	1.141	4.298
LP-AD-HPSC	0.863	1.036	3.907
LW-AD-$scCO_2$	0.896	1.041	4.217
LW-AD-HPSC	1.329	1.557	5.683
LP-WQ-$scCO_2$	1.415	1.592	5.503
LP-WQ-HPSC	0.538	0.648	2.661
LW-WQ-$scCO_2$	0.787	0.985	4.321
LW-WQ-HPSC	0.644	0.847	3.796

The light microscope observations and roughness profiles of the machined surface of as-deposited (AD) samples, shown in Figure 31, reveal slight differences between samples. According to the roughness measurements, LP-AD-$scCO_2$, LP-AD-HPSC, and LW-AD-$scCO_2$ samples present similar roughness, while the LW-AD-HPSC sample demonstrates higher roughness. These results agree with light microscope observations and roughness profiles, showing the highest roughness LW-AD-HPSC (Figure 31(d)).

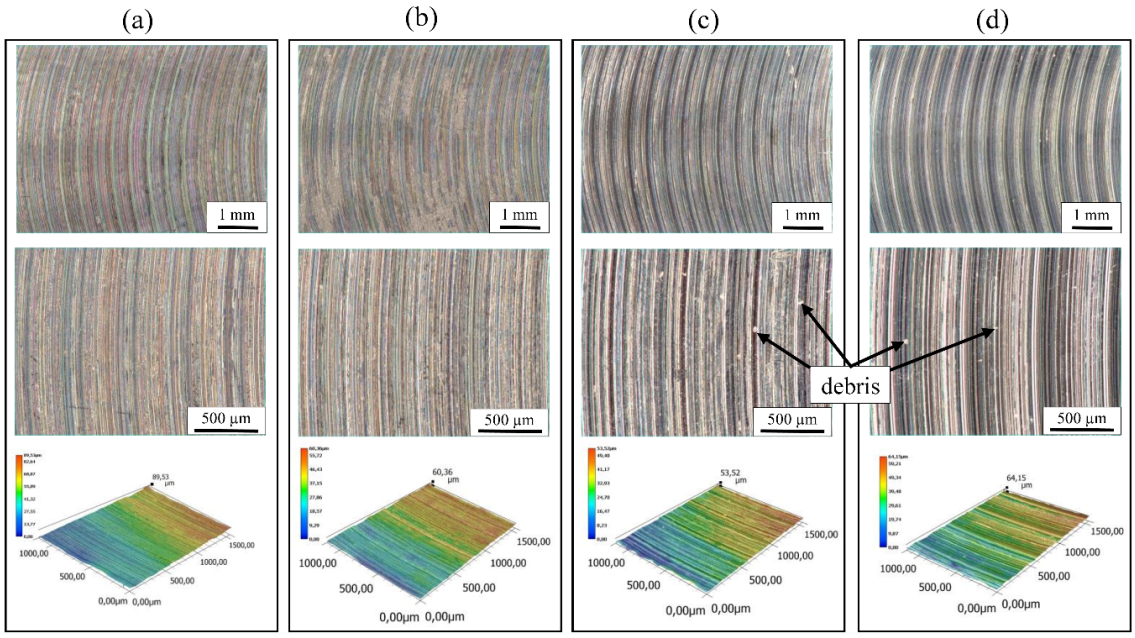

Figure 31: Light microscope observations of machined together with roughness profiles: (a) LP-AD-$scCO_2$, (b) LP-AD-HPSC, (c) LW-AD-$scCO_2$, and d) LW-AD-HPSC.

The light microscope images and roughness profiles of the machined surface of annealed and WQ samples are shown in Figure 32. The results agree with roughness measurements, revealing that the LP-WQ-HPSC sample shows the lowest roughness. It should be noted that in both AD and WQ samples, differences in feed mark width were found. In the samples produced from the wire feedstock (LW), feed marks seem to be broader than in the samples produced from the powder feedstock (LP). Moreover, in the LW samples, debris was found reattached to the machined surface (Figure 31(c), Figure 31(d), Figure 32(c), and Figure 32(d), and is known to increase localised hardness.

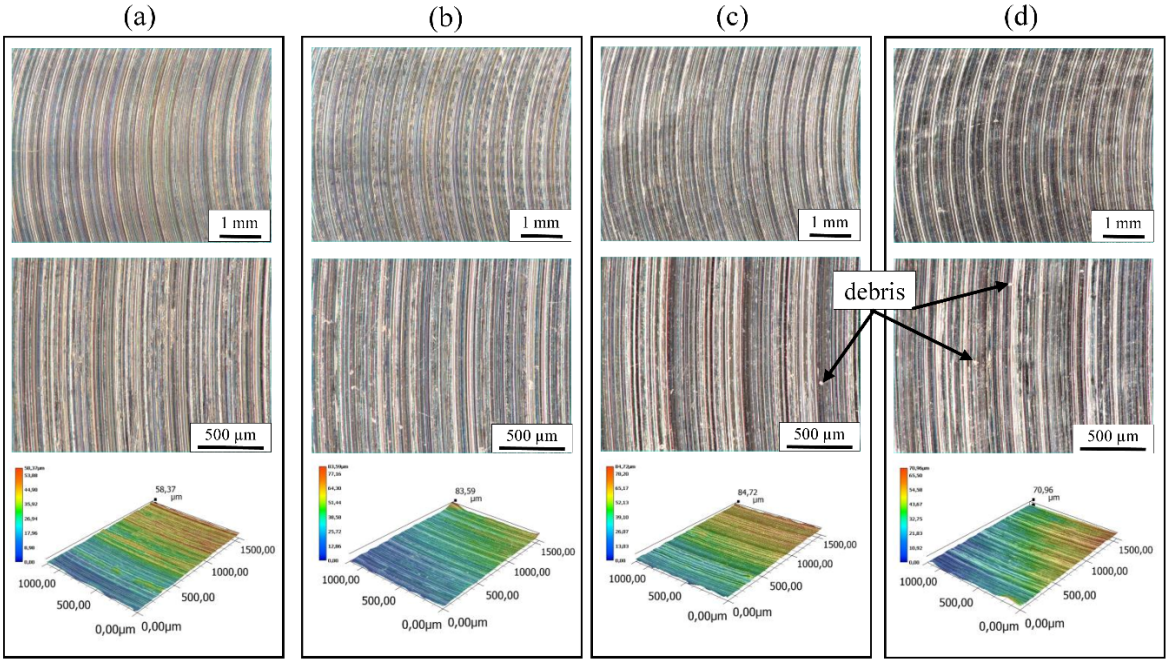

Figure 32: Light microscope observations of machined together with roughness profiles: a) LP-WQ-scCO$_2$, b) LP-WQ-HPSC, c) LW-WQ-scCO$_2$, and d) LW-WQ-HPSC.

SEM images of the cross-section of the machined samples could deliver qualitative information about deformation induced by machining. The performed analyses, shown in Figure 33, reveal that the deformation is visible in all studied samples. However, the deformation is the most visible in LW-AD-scCO$_2$, LW-AD-HPSC, and LP-WQ-scCO$_2$. Moreover, the LW-AD-HPSC and LP-WQ-scCO$_2$ samples reveal the highest roughness (Table 8); therefore, it seems that the processing of these samples should be modified.

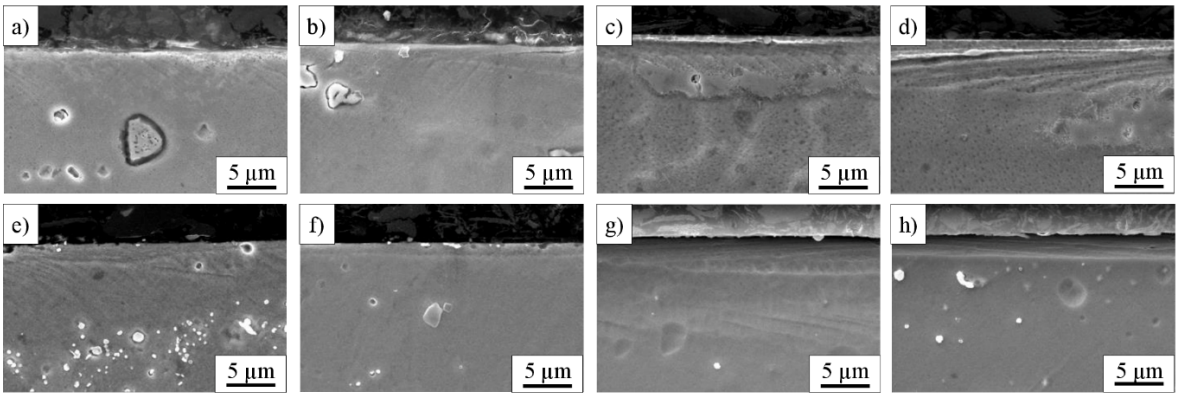

Figure 33: SEM observations of a cross-section of the machined samples: a) LP-AD-scCO$_2$, b) LP-AD-HPSC, c) LW-AD-scCO$_2$, d) LW-AD-HPSC, e) LP-WQ-scCO$_2$, f) LP-WQ-HPSC, g) LW-WQ-scCO$_2$, and h) LW-WQ-HPSC.

EBSD data of the cross-section of machined samples could deliver more precise data about the work hardening due to deformation caused by machining than simple SEM imaging. According to the EBSD performed in this study, shown in Figure 34 and Figure 35, the deformation is visible on inverse pole figure (IPF) maps. In most samples, the depth of the deformed layer is about 50 µm. However, in the LP-AD-HPSC, the deformed layer seems to be much larger, up to 100 µm. It should be noted that the machining process does not change the texture of the samples.

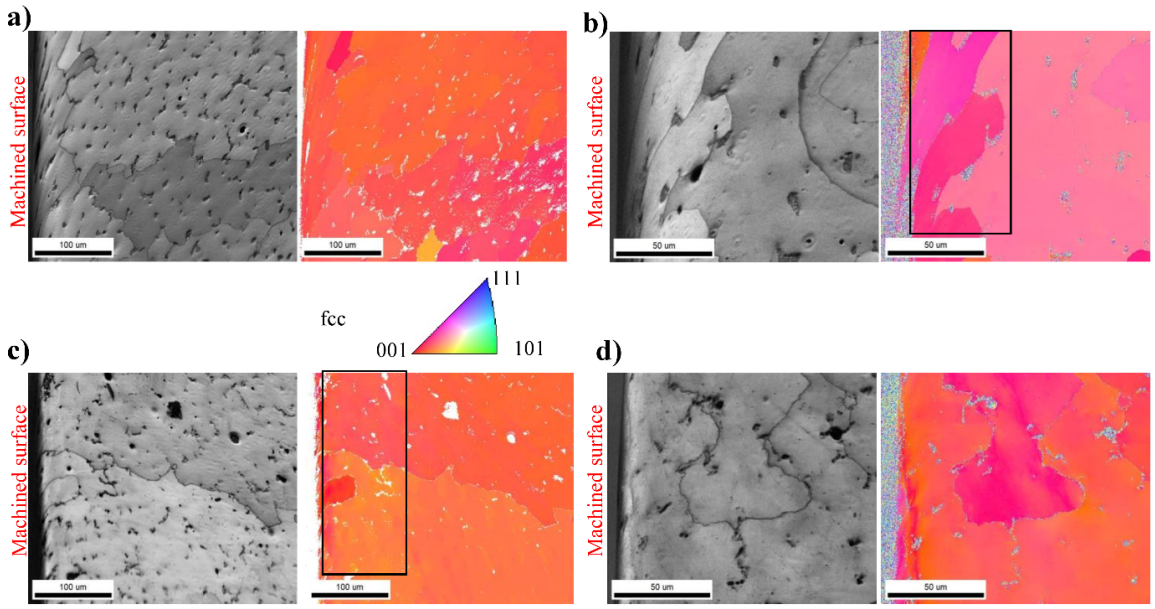

Figure 34:EBSD analyses (image quality (IQ) and inverse pole figure (IPF) image) of the cross-section of machined LP-AD samples: a) lower magnification of LP-AD-scCO₂ sample, b) higher magnification of LP-AD-scCO₂ sample with marked zone of the most significant deformation, c) lower magnification of LP-AD-HPSC sample with marked zone of the most significant deformation, and d) higher magnification of LP-AD-HPSC sample.

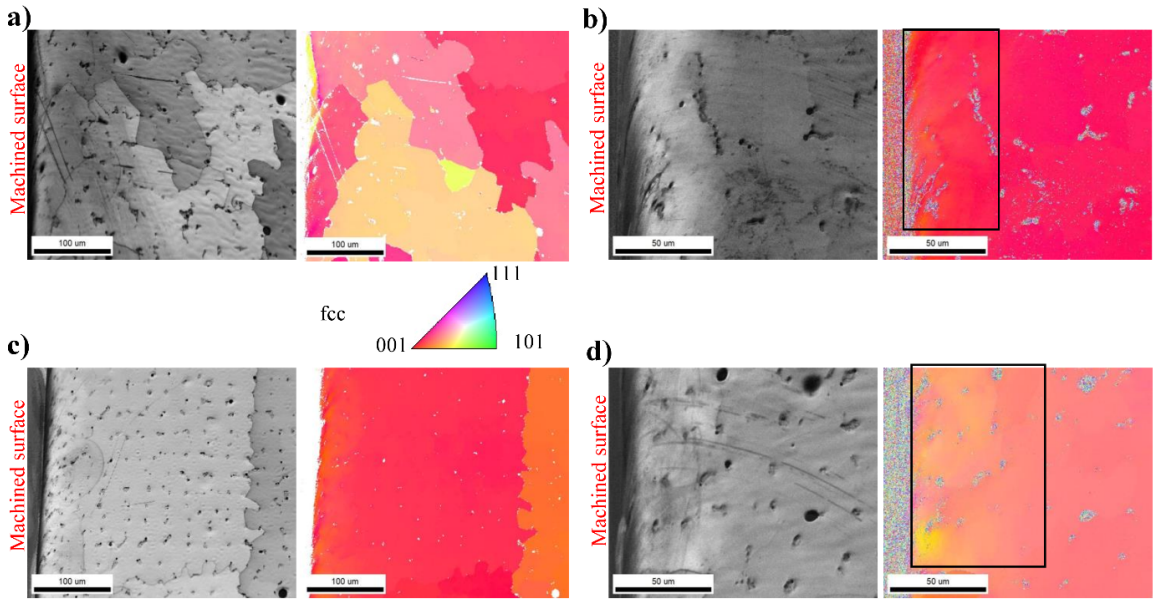

Figure 35:EBSD analyses (image quality (IQ) and inverse pole figure (IPF) image) of the cross-section of machined LP-WQ samples: a) lower magnification of LP-WQ-scCO₂ sample, b) higher magnification of LP-WQ-scCO₂ sample with marked zone of the most significant deformation, c) lower magnification of LP-WQ-HPSC sample, and d) higher magnification of LP-WQ-HPSC sample with marked zone of the most significant deformation.

The microhardness measurements performed in the centre of the samples (far from the deformation induced by machining) show small differences in hardness among samples. Samples produced from powder feedstock reveal slightly lower hardness. Moreover, annealing followed by water quenching reduces the hardness slightly. This slight decrease in hardness could result from a smaller volume fraction, and size of Cr-rich and Mo-rich carbides in the samples produced from wire feedstock and samples after annealing.

The microhardness distribution measurements on the cross-section of the samples reveal a significant increase in hardness near the machined surface. The plots of microhardness distribution are shown in Figure 36. The microhardness near surfaces (10 µm from the surface) increases by 38-47% compared to the value measured in the centre of the sample (Table 9). At 100 µm in-depth, the hardness is similar to the centre of the sample. These results agree with EBSD (Figure 34 and Figure 35), revealing that the visible deformed layers have a thickness of approximately 50 µm in most samples. The highest hardness of 348±17 HV at 10 µm from the machined surface was found in the LP-AD-HPSC sample. It corresponds to a 47% increase in hardness compared to the centre of the sample, which is the most significant among the studied samples. The results are in agreement with EBSD results (Figure 34(c) and Figure 34(d)), showing the most considerable deformation layer, up to 100 µm in this sample. Moreover, the results show no significant impact of cooling strategy (HPSC vs $scCO_2$) on microhardness distribution. The differences between HPSC and $scCO_2$ are somewhat in the margin of error. However, the samples cooled by $scCO_2$ during machining show slightly lower hardness near the machined surface (Table 9).

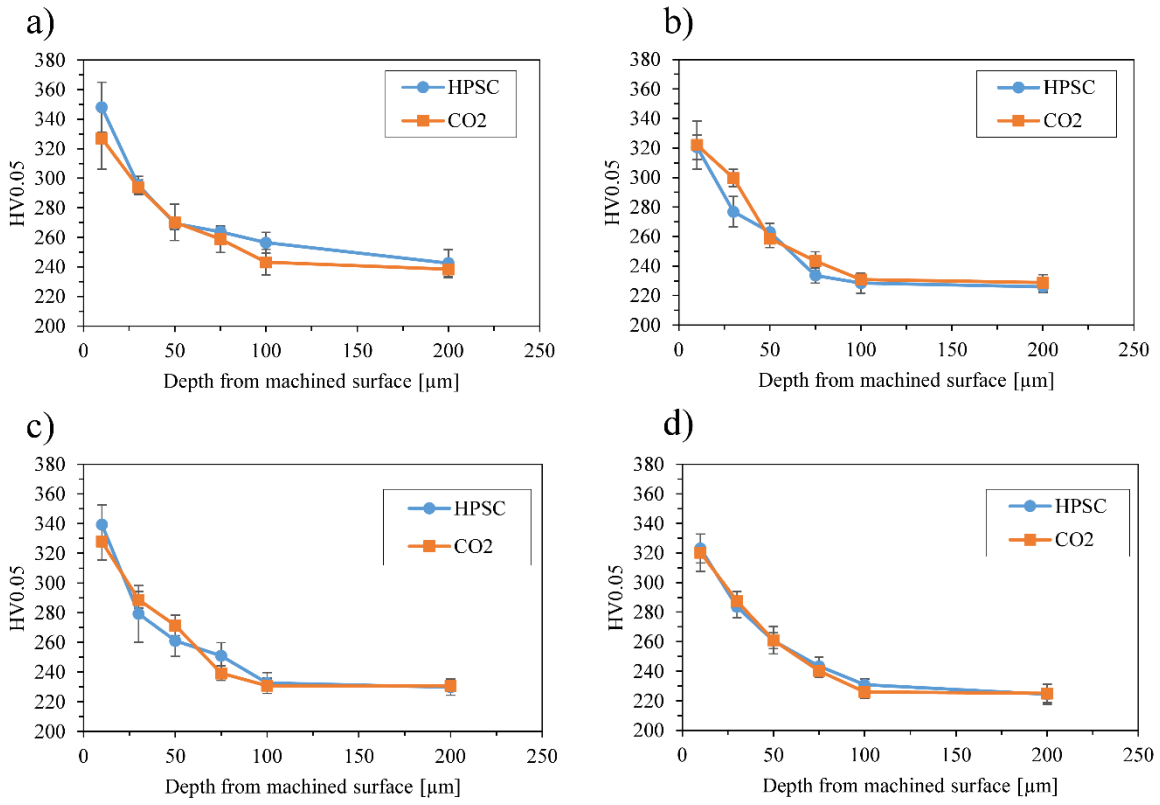

Figure 36: Microhardness distribution measurements on the cross-section of machined samples using two different cooling strategies ($scCO_2$+MQL or HPSC) a) LP-AD, b) LW-AD, c) LP-WQ, and d) LW-WQ.

Table 9: Results summarising microhardness increase near the machined surface.

Sample	Hardness in the center of the cross-section [HV0.05]	Increase of hardness on the cross-section at 10 µm in depth from the machined surface [%]
LP-AD-scCO$_2$	237±12	38%
LP-AD-HPSC		47%
LW-AD-scCO$_2$	229±5	41%
LW-AD-HPSC		41%
LP-WQ-scCO$_2$	230±6	43%
LP-WQ-HPSC		47%
LW-WQ-scCO$_2$	227±4	41%
LW-WQ-HPSC		42%

The presented results facilitate better understanding of the effects of machining under different cooling strategies on the surface integrity of Inconel 617 alloy produced from wire or powder feedstock and subjected to different heat treatment procedures. The obtained roughness (Ra) values between 0.538 and 1.415 µm, and related surface observations reveal low roughness and good surface quality. However, debris was found in the samples prepared from wire feedstock. The microhardness results reveal nominal differences between the cooling strategy (HPSC vs. scCO$_2$) and the small impact of post-deposition heat treatment. The microhardness is significantly higher in the vicinity of the machined surface, which was attributed to deformation induced during machining (work hardening). The EBSD observations confirm the presence of a deformed layer, at approximately 50 µm for most samples.

4.4 Outcomes and development prospects

The objective of this work was to assess the suitability of selected processes for the design and construction of GFRs. Specifically, the focus was on the manufacturing of different materials that can potentially overcome the challenges of GFR design. From this perspective, the selected processes were successfully used to derive representative AM material samples from Inconel alloy 617. These material samples were used to support feasibility assessment studies and provided insights into specific areas to be further investigated. These include the suitability of the target GFR component designs for AM, the compatibility of different AM technologies, and the research and development scope, including the time and resources needed to achieve design and construction equivalence, when adopting AM technologies. Related considerations, include the skills and expertise needed for industrial processes, notwithstanding the process effectiveness, product functionality and durability, as well as the safety and certification requirements. Nevertheless, the preliminary findings from the processing of alloy 617 provide a basis on which a development strategy may be formulated. The aim is to support feasibility assessments, enabled by clearly defined qualitative and quantitative metrics.

Off-the-shelf tooling and inserts were used for machinability investigations, which involved the evaluation of HPSC and scCO$_2$+MQL cooling strategies for the machining of AM Inconel 617 materials. Ra values of less than 1.6 µm were measured, with nearly all values (93.75%) conforming to aerospace specifications with Ra values of < 1.6 µm. Although the sampling rate was low, when comparing surface roughness and cutting force data, it was observed that the scCO$_2$+MQL cooling strategy generally resulted in lower roughness values when compared to samples machined using the HPSC. Correspondingly, it appeared that cutting forces remained stable even with non-ideal thin section samples. Furthermore, there appeared to be correlations between the material condition and surface roughness, with higher values typically obtained from samples machined in the as-deposited condition. The cooling rate between the heat-treated samples was also observed to influence the material condition, with faster WQ typically resulting in higher roughness values, and slower FC resulting in

lower roughness values. Overall, the machined surfaces of DED-LP samples were observed to be relatively smoother than the DED-LW samples. This observation was corroborated by the tool inspection data, which revealed that all laser wire samples (DED-LW) had at least one insert with a chip on the cutting-edge of the tool, while there was no chipping on any of the inserts used for machining the DED-LP samples. There were more mixed results obtained when comparing the microhardness and machining data, but the results were generally consistent with roughness data, whereby rapid cooling (i.e., WQ) resulted in higher values, relative to slow cooling procedures (i.e., FC), and measurements obtained from DED-LW samples were often higher than that obtained from DED-LP samples. Based on these initial results, the machining of more dimensionally identical and dynamically stable material samples, and representative components, to gather more relevant application data, is necessary to obtain further machinability insights. These investigations would significantly enrich the data pool and thus enhance confidence in the reliability of the information on which decisions are based regarding the different processes and procedures.

Fundamentally, the focus of this subtask was to determine a processing window for alloy 617, which was achieved, allowing for the fabrication of representative materials from each of the selected processes, and the manufacturing of the SafeG demonstrator. However, further investigation is necessary to refine the processing approach and related procedures, and fully quantify all relevant macro and micro characteristics and mechanical properties, considering the safety, performance and durability of the targeted applications for these technologies.

5 CONCLUSIONS

The aim of this task was to investigate how innovative materials may be introduced into the design of GFRs, particularly ALLEGRO, and assess the suitability of innovative processing technologies for manufacturing these materials, including FeCrAl-ODS alloys and Inconel 617 alloys. The investigation of FeCrAl-ODS was enabled by the MA technique, which was used to create eight compositions of FeCrAl-based ODS alloys, with Y_2O_3 oxide and V, Ti additions selected. These promising outputs exhibited excellent mechanical properties at elevated temperatures that were close to the operating temperatures specified for ALLEGRO. Correspondingly, additive manufacturing is very promising for fabricating components for the nuclear industry, and DED and LPBF methods were investigated for the AM of Inconel alloy 617, with the DHR HX component selected as a use case, to explore the benefits and limitations of this approach. Different AM systems, including both the powder and wire feedstocks, and laser and arc energy sources, were used to successfully demonstrate the feasibility of this processing approach. The machinability of the resulting alloy 617 material samples was also evaluated using different cooling strategies, and the results are promising, with low roughness and a small deformation zone observed after machining.

The purpose of this study was to assess the possibility of manufacturing components from the selected materials. This objective was achieved via the SafeG demonstrator, which was additively manufactured from alloy 617. The goal of identifying advanced manufacturing processes to enable design of key safety-related components of GFRs is equally important, and it was demonstrated that to varying degrees, all processes investigated can enable GFR components manufacture. In particular, the identification, selection, and investigation of distinct technologies, during the processing of both FeCrAl-ODS and Inconel 617 alloys yielded significant data, which will enhance understanding of the critical factors and directly inform decisions regarding future research prospects and specific actions for ALLEGRO. Correspondingly, while AM was shown to be effective for the manufacture of the scaled DHR HX component, the suitability of these technologies, for Generator IV reactor applications, would have to be established via a defined equipment qualification test regime, conducted to the applicable standards.

References

[1] Z. Hózer, T. Hinoki, E. Slonszki, A. Pintér-Csordás, L. Illés, M. Király, et al. SafeG_D2_1_ Innovative cladding materials testing. 2022.
[2] P. Vácha, J. Komrska, J. Pokorný, R. Koryčanský. SafeG_D2_3_ DHR Heat Exchanger. 2023.
[3] Abram T, Ion S. Generation-IV nuclear power: a review of the state of the science. Energy Policy 2008;36:4323–30. https://doi.org/10.1016/j.enpol.2008.09.059.
[4] Yvon P, Carré F. Structural materials challenges for advanced reactor systems. J Nucl Mater 2009;385:217–22. https://doi.org/10.1016/j.jnucmat.2008.11.026.
[5] Meza A, Macía E, Chekhonin P, Altstadt E, Rabanal ME, Torralba JM, et al. The effect of composition and microstructure on the creep behaviour of 14 Cr ODS steels consolidated by SPS. Mater Sci Eng A 2022;849:143441. https://doi.org/10.1016/j.msea.2022.143441.
[6] Terrani KA. Accident tolerant fuel cladding development: promise, status, and challenges. J Nucl Mater 2018;501:13–30. https://doi.org/10.1016/j.jnucmat.2017.12.043.
[7] Field KG, Snead MA, Yamamoto Y, Terrani KA. Handbook on the material properties of FeCrAl alloys for nuclear power production applications. Nucl Technol Res Dev 2017.
[8] Edgren A. High temperature corrosion of FeCrAl alloys in humidified environment 2019.
[9] Li W, Lu S, Hu Q-M, Mao H, Johansson B, Vitos L. The effect of Al on the 475 °C embrittlement of Fe–Cr alloys. Comput Mater Sci 2013;74:101–6. https://doi.org/10.1016/j.commatsci.2013.03.021.
[10] Capdevila C, Aranda MM, Rementeria R, Domínguez-Reyes R, Urones-Garrote E, Miller MK. Influence of nanovoids on α–α′ phase separation in FeCrAl oxide dispersion strengthened alloy. Scr Mater 2016;110:53–6. https://doi.org/10.1016/j.scriptamat.2015.07.044.
[11] Wang J, Long D, Yu L, Liu Y, Li H, Wang Z. Influence of Al addition on the microstructure and mechanical properties of Zr-containing 9Cr-ODS steel. J Mater Res Technol 2021;13:1698–708. https://doi.org/10.1016/j.jmrt.2021.05.112.
[12] Ohtsuka S, Kaito T, Inoue M, Asayama T, Kim SW, Ukai S, et al. Effects of aluminum on high-temperature strength of 9Cr–ODS steel. J Nucl Mater 2009;386–388:479–82. https://doi.org/10.1016/j.jnucmat.2008.12.147.
[13] Oksiuta Z, Lewandowska M, Kurzydlowski KJ, Baluc N. Effect of vanadium addition on the microstructure and mechanical properties of the ODS ferritic steels. J Nucl Mater 2013;442:S84–8. https://doi.org/10.1016/j.jnucmat.2012.10.022.
[14] Yang T-X, Li Z-X, Zhou C-J, Xu Y-C, Dou P. Effects of Zr and/or Ti addition on the morphology, crystal and metal/oxide interface structures of nanoparticles in FeCrAl-ODS steels. J Nucl Mater 2023;585:154613. https://doi.org/10.1016/j.jnucmat.2023.154613.
[15] Massey CP, Edmondson PD, Unocic KA, Yang Y, Dryepondt SN, Kini A, et al. The effect of Zr on precipitation in oxide dispersion strengthened FeCrAl alloys. J Nucl Mater 2020;533:152105. https://doi.org/10.1016/j.jnucmat.2020.152105.
[16] Wang X, Lu Z, Li Z, Shi Y, Xu H. Effect of Zr content on microstructure and hardness of ODS-FeCrAl alloys. Mater Charact 2022;192:112221.
[17] Frelek-Kozak M, Kurpaska L, Wyszkowska E, Jagielski J, Pawlak W, Jozwik I, et al. Influence of consolidation process on functional properties of steels. Surf Coat Technol 2018;355:234–9.
[18] Frelek-Kozak M, Kurpaska Ł, Mulewska K, Zieliński M, Diduszko R, Kosińska A, et al. Mechanical behavior of ion-irradiated ODS RAF steels strengthened with different types of refractory oxides. Appl Surf Sci 2023;610:155465. https://doi.org/10.1016/j.apsusc.2022.155465.
[19] Kurpaska L, Jozwik I, Lewandowska M, Jagielski J. The effect of Ar-ion irradiation on nanomechanical and structural properties of ODS RAF steels manufactured by using HIP technique. Vacuum 2017;145:144–52. https://doi.org/10.1016/j.vacuum.2017.08.039.
[20] Wyszkowska E, Kurpaska L, Frelek-Kozak M, Jozwik I, Perkowski K, Jagielski J. Investigation of the mechanical properties of ODS steels at high temperatures using nanoindentation technique. Nucl Instrum Methods Phys Res Sect B Beam Interact Mater At 2019;444:107–11. https://doi.org/10.1016/j.nimb.2019.02.021.
[21] Kobayashi S, Takasugi T. Mapping of 475 °C embrittlement in ferritic Fe–Cr–Al alloys. Scr Mater 2010;63:1104–7. https://doi.org/10.1016/j.scriptamat.2010.08.015.
[22] Han W, Yabuuchi K, Kimura A, Ukai S, Oono N, Kaito T, et al. Effect of Cr/Al contents on the 475 ° C age-hardening in oxide dispersion strengthened ferritic steels. Nucl Mater Energy 2016;9:610–5. https://doi.org/10.1016/j.nme.2016.05.015.

[23] García-Junceda A, Macía E, Garbiec D, Serrano M, Torralba JM, Campos M. Effect of small variations in Zr content on the microstructure and properties of ferritic ODS steels consolidated by SPS. Metals 2020;10:348.
[24] Boulnat X, Perez M, Fabregue D, Douillard T, Mathon M-H, De Carlan Y. Microstructure evolution in nano-reinforced ferritic steel processed by mechanical alloying and spark plasma sintering. Metall Mater Trans A 2014;45:1485–97. https://doi.org/10.1007/s11661-013-2107-y.
[25] Munir ZA, Anselmi-Tamburini U, Ohyanagi M. The effect of electric field and pressure on the synthesis and consolidation of materials: a review of the spark plasma sintering method. J Mater Sci 2006;41:763–77. https://doi.org/10.1007/s10853-006-6555-2.
[26] Li Y, Shen J, Li F, Yang H, Kano S, Matsukawa Y, et al. Effects of fabrication processing on the microstructure and mechanical properties of oxide dispersion strengthening steels. Mater Sci Eng A 2016;654:203–12. https://doi.org/10.1016/j.msea.2015.12.032.
[27] Macía E, García-Junceda A, Serrano M, Hernández-Mayoral M, Diaz LA, Campos M. Effect of the heating rate on the microstructure of a ferritic ODS steel with four oxide formers (Y-Ti-Al-Zr) consolidated by spark plasma sintering (SPS). J Nucl Mater 2019;518:190–201. https://doi.org/10.1016/j.jnucmat.2019.02.043.
[28] Chen C-L, Dong Y-M. Effect of mechanical alloying and consolidation process on microstructure and hardness of nanostructured Fe–Cr–Al ODS alloys. Mater Sci Eng A 2011;528:8374–80. https://doi.org/10.1016/j.msea.2011.08.041.
[29] Dash MK, Mythili R, Ravi R, Sakthivel T, Dasgupta A, Saroja S, et al. Microstructure and mechanical properties of oxide dispersion strengthened 18Cr-ferritic steel consolidated by spark plasma sintering. Mater Sci Eng A 2018;736:137–47. https://doi.org/10.1016/j.msea.2018.08.093.
[30] Das A, Chekhonin P, Altstadt E, McClintock D, Bergner F, Heintze C, et al. Microstructure and fracture toughness characterization of three 9Cr ODS EUROFER steels with different thermo-mechanical treatments. J Nucl Mater 2020;542:152464.
[31] Sang W, Dou P, Kimura A. Early-stage thermal ageing behavior of 12Cr, 12Cr–7Al and 18Cr–9Al ODS steels. J Nucl Mater 2020;535:152164. https://doi.org/10.1016/j.jnucmat.2020.152164.
[32] Jang K-N, Kim T-K, Kim K-T. The effect of cooling rates on carbide precipitate and microstructure of 9CR-1MO oxide dispersion strengthened(ODS) steel. Nucl Eng Technol 2019;51:249–56. https://doi.org/10.1016/j.net.2018.09.021.
[33] Adamiec J, Konieczna N. Assessment of the hot cracking susceptibility of the inconel 617 nickel-based alloy. Arch Metall Mater 2021;66.
[34] Ravibharath R, Devakumaran K, Muthupandi V. Studies on susceptibility of alloy 617 to solidification cracking. Mater. Sci. Forum, vol. 969, Trans Tech Publ; 2019, p. 34–40.
[35] Sathish T, Arul K, Subbiah R, Ravichandran M, Mohanavel V. Optimization on end milling operating parameters for super alloy of inconel 617 by taguchi's L27 orthogonal array. J. Phys. Conf. Ser., vol. 2027, IOP Publishing; 2021, p. 12013.
[36] Venkatesan K, Mathew AT, Devendiran S, Ghazaly NM, Sanjith S, Raghul R. Machinability study and multi-response optimization of cutting force, surface roughness and tool wear on CNC turned inconel 617 superalloy using Al2O3 nanofluids in coconut oil. Procedia Manuf 2019;30:396–403. https://doi.org/10.1016/j.promfg.2019.02.055.
[37] Miller K. Special Metal Technical Bulletin - Inconel Alloy617 2005.
[38] VDM® Alloy 617 Material Data Sheet No. 4119 2022.
[39] Technical Guide - Machining Nickel Alloys (11008) 2022.
[40] Benga G, Veldhuis S. Influence of cutting parameters on the cutting forces when slotting inconel 617. Proc. 15th Int. Conf. Manuf. Syst. – ICMaS, Bucharest, Romania: Editura Academiei Române; 2006, p. 287–90.
[41] American Society of Mechanical Engineers Standards Committee B46 Classification, Designation of Surface Qualities, American National Standards Institute. Surface texture: surface roughness, waviness and lay. American Society of Mechanical Engineers; 2003.
[42] Xiuqing L, Le Pierres R, Dewson SJ. Heat exchangers for the next generation of nuclear reactors. American Nuclear Society - ANS, La Grange Park (United States); 2006.
[43] Kaynak Y, Tascioglu E. Finish machining-induced surface roughness, microhardness and XRD analysis of selective laser melted inconel 718 alloy. Procedia CIRP 2018;71:500–4. https://doi.org/10.1016/j.procir.2018.05.013.

[44] Kaynak Y, Kitay O. Porosity, surface quality, microhardness and microstructure of selective laser melted 316L stainless steel resulting from finish machining. J Manuf Mater Process 2018;2:36. https://doi.org/10.3390/jmmp2020036.